

Madeleine I. Frank

**Unusually Hydrous High-Mg Basanites and Minettes of the
Kings River Volcanic Field, Sierra Nevada, CA**


submitted in partial fulfillment of the requirements for the degree of

Master of Science in Earth and Environmental Sciences

Department of Earth and Environmental Sciences

The University of Michigan

Accepted by:

_____ Signature	Becky Lange Apr. Electronically _____	_____ Name	Becky Lange	_____ Date	8/21/2023
_____ Signature	Adam Simon	_____ Name	Adam Simon	_____ Date	8/21/2023
_____ Department Chair Signature		_____ Name	Julia Cole	_____ Date	8/21/2023

I hereby grant the University of Michigan, its heirs and assigns, the non-exclusive right to reproduce and distribute single copies of my thesis, in whole or in part, in any format. I represent and warrant to the University of Michigan that the thesis is an original work, does not infringe or violate any rights of others, and that I make these grants as the sole owner of the rights to my thesis. I understand that I will not receive royalties for any reproduction of this thesis.

- Permission granted.
- Permission granted to copy after: _____
- Permission declined.

Author Signature



ABSTRACT

A collection of Pliocene, high-MgO (≤ 14 wt%) basanite and minette flows, with an enhanced arc geochemical signature, are located near the North, Middle and South Forks of the Kings River in the southern Sierra Nevada, CA. The Kings River volcanic field broadly overlies the boundary (defined by lithospheric-scale thrusts) between accreted oceanic lithosphere (Panthalassa) and Proterozoic North America (e.g., Kistler, 1990; Saleeby, 2011). In this study, the high-MgO (≤ 15.4 wt%) character of the Kings River suite is shown to reflect liquid compositions, consistent with evidence that their phenocrysts grew during rapid ascent to the surface via dikes (and not in a crustal magma chamber). For eight of ten samples, the most Mg-rich analyzed olivine matches the equilibrium composition at the liquidus. For the other two samples, it is the most Mg-rich analyzed clinopyroxene that passes the equilibrium liquidus test. Application of clinopyroxene-melt barometry (Neave and Putirka, 2017) to these two samples indicates the onset of phenocryst growth at ~ 0.5 GPa. Application of coupled Mg- and Ni-based olivine-melt thermometry (Pu et al., 2017) to the other eight Kings River samples provides the temperature and dissolved H₂O content at the liquidus. Because the Mg-thermometer is sensitive to dissolved H₂O in the melt, its application without a correction for H₂O gives the temperature of olivine crystallization under anhydrous conditions. In contrast, because the Ni-thermometer is insensitive to dissolved H₂O, it gives the actual temperature of olivine crystallization under hydrous conditions without a water correction. For the eight Kings River samples with olivine on the liquidus, resulting temperatures range from 1220-1047 °C. When the Mg- and Ni-based temperatures are paired, the depression of the liquidus ($\Delta T = T_{\text{Mg}} - T_{\text{Ni}}$) ranges from 234-129 °C (average is 186 °C). An updated model calibration that relates ΔT with dissolved H₂O in the melt (Pu et al., 2023) gives 6.1-11.0 wt% (average is 8.8 wt%) H₂O for the Kings River suite. An

outstanding question is how the Kings River melts attained such high-water contents in the absence of an active subduction zone. Previous studies have proposed that lithospheric delamination may have triggered formation of the Kings River volcanic suite, which is isotopically constrained to be derived from subduction-modified Proterozoic mantle (e.g., Manley et al., 2000; Farmer et al., 2002). Here, we propose that delamination may have involved serpentinized Panthalassan lithosphere, which released H₂O-rich fluid into the Proterozoic lithospheric source for the Kings River volcanic suite.

INTRODUCTION

An unusual suite of K-rich Pliocene basanites and minettes, with an enhanced arc geochemical signature, erupted through the southern Sierra Nevada batholith adjacent to the Kings River watershed (Fig. 1). Seismic evidence shows that lithospheric delamination is occurring beneath the southern Sierra Nevada, leading to upwelling of warm asthenosphere (e.g., Ruppert et al., 1998; Zandt et al., 2004; Frassetto et al., 2011; Gilbert et al., 2012). Studies of mafic lower-crustal and mantle xenoliths entrained in Sierran volcanic rocks shows that lithosphere delamination initiated sometime between 10-3 Ma (e.g., Ducea and Saleeby, 1996). The abrupt pulse (~3.5 Ma) of Pliocene K-rich volcanism in the southern Sierra Nevada has led some researchers to hypothesize that foundering of the lithosphere triggered the formation of these unusual melts (e.g., Manley et al., 2000; Farmer et al., 2002).

The Kings River basanites and minettes are also notable for their remarkably high MgO contents (≤ 15 wt%; Feldstein and Lange, 1999; Farmer et al., 2002), which raises several questions including whether they represent liquid compositions or instead reflect the accumulation of olivine phenocrysts and/or xenocrysts. In this study, equilibrium exchange

partition coefficients involving Fe^{2+} -Mg and Mn-Mg between olivine and melt are employed to address this question. More specifically, we test the hypothesis that the most Mg-rich analyzed phenocryst in each sample (olivine and/or clinopyroxene) represents the first phase to crystallize at the liquidus of a melt with the whole-rock composition. For Kings River samples that pass this test (i.e., are shown to represent liquid compositions), a related question is whether their successful eruption through >30 km of granitoid crust indicates that they ascended rapidly, via dikes, without stalling in crustal magma chambers.

If the Kings River volcanic samples are shown to represent liquid compositions, the next question is whether unusually high temperatures and/or unusually high H_2O contents were required to generate such high-MgO melts from their mantle source (i.e., through high melt fractions of lherzolite and/or melting of a relatively refractory, though subduction-modified, harzburgitic lithosphere). To address this question, the olivine-melt thermometer and hygrometer of Pu et al. (2017), which are based on the partitioning of Ni and Mg between olivine and melt ($D_{\text{Ni}}^{\text{ol/liq}}$ and $D_{\text{Mg}}^{\text{ol/liq}}$), are applied to the Kings River lavas.

The advantage of the $D_{\text{Ni}}^{\text{ol/liq}}$ thermometer is that it is independent of dissolved H_2O content in the melt (Pu et al., 2021), which differs from Mg-based olivine-melt thermometers (e.g., Beattie et al., 1993). It is well known from the literature that $D_{\text{Mg}}^{\text{ol/liq}}$ is strongly dependent on the amount of dissolved H_2O in the melt (Putirka et al., 2007), and if it is applied without an H_2O correction, the calculated temperature gives the olivine crystallization under anhydrous conditions. In contrast, dissolved H_2O in the melt has no effect on the Ni-based olivine-melt thermometer (Pu et al., 2021), and therefore no H_2O correction is required for the Ni-thermometer. As a result, application of the Ni-thermometer to hydrous basalts gives the actual

temperature of olivine crystallization under hydrous conditions, without the requirement to know the H₂O content in the melt.

Because the Mg-thermometer effectively provides the temperature under anhydrous conditions (irrespective of how much H₂O is in the melt), application of both the Ni- and Mg-thermometers (calibrated on the same experimental dataset; Pu et al., 2017) gives the depression of the olivine liquidus temperature due to dissolved H₂O in the melt ($\Delta T = T_{\text{anhydrous}} - T_{\text{hydrous}} = T_{\text{Mg}} - T_{\text{Ni}}$). An updated experimental calibration that relates the depression of the olivine liquidus (ΔT) with dissolved water in the melt (Pu et al., 2023) can be used to calculate melt water contents.

In this study, the thermometry and hygrometry results obtained for the Kings River volcanic suite are compared to those previously reported for the Pliocene Long Valley basalts (Jolles and Lange, 2021) and the Quaternary Big Pine basalts (Brehm and Lange, 2020), both erupted along the eastern escarpment of the Sierra Nevada (Fig. 1). The results will be combined with isotopic constraints from the literature to evaluate what conditions in their respective mantle sources led to the unusual compositions of the Kings River lavas compared to the Long Valley and Big Pine basalts.

TECTONIC SETTING

The Kings River volcanic field erupted through the Sierra Nevada granitoid batholith, which formed over a prolonged period (~220-80 Ma) of Mesozoic subduction of the Farallon oceanic plate beneath the North American continental plate. Immediately to the west, in the foothills of the Sierra Nevada, is the Kings River ophiolite belt, which formed at ~484 Ma within the Panthalassa ocean basin (Saleeby, 1982; Shaw et al., 1987). During the Permo-

Carboniferous (~300 Ma), the Kings River ophiolite belt, along with other correlative ophiolitic members along the western Sierran foothills, was emplaced along a strike-slip boundary that truncated the passive margin of southwestern North America (e.g., Saleeby, 1992, 2011; Dickinson and Lawton, 2001). By ~255 Ma, this transform boundary had evolved into a neo-subduction zone, along which the ophiolitic assemblages (which included serpentinites), were emplaced as a proto-forearc wedge (Saleeby, 2011). This incipient convergent margin then evolved into the Mesozoic subduction zone that created the Sierra Nevada granitoid batholith. This tectonic history created the boundary between younger (Paleozoic) oceanic, Panthalassan lithosphere and older (Proterozoic) continental North American lithosphere, which is broadly recorded in the Sierra Nevada by the >0.706 $^{87}\text{Sr}/^{86}\text{Sr}$ line of Kistler (1990) and underlies the Kings River volcanic field (Fig. 1a).

The long duration of Mesozoic subduction of nearly 140 m.y. led to a Sierra Nevada crustal column that was at least 70 km thick, which is confirmed by the presence of lower-crustal xenoliths in the eclogite facies that erupted in Miocene Sierran volcanic rocks (Ducea and Saleeby, 1996, 1998a,b). Between ~80-40 Ma, flat subduction shut off Sierran arc magmatism, and by ~40-30 Ma, the arrival of the Pacific-Farallon spreading ridge at the subduction trench led to the development of the San Andreas strike-slip plate boundary (Atwater, 1970). This tectonic transition produced a slab window beneath the southern Sierra Nevada at ~20 Ma, which was well developed by ~13 Ma (Atwater and Stock, 1998).

Various seismic surveys (Rupert et al., 1998; Fleidner et al., 2000; Zandt et al., 2004; Frassetto et al., 2011; Gilbert et al., 2012) show that the Sierran arc crust beneath the Kings River volcanic field is currently ~35-40 km thick, only half its Cretaceous thickness. Moreover, most of the crustal column is made of granitoid, indicating that the dense batholithic root (i.e.,

eclogite-facies, mafic crust) and at least part of the underlying lithospheric mantle has delaminated and/or degraded. Although there is no direct information on the timing of lithosphere removal and/or degradation beneath the southern Sierra, several studies point to the abrupt pulse (~3.4-3.6 Ma) of Pliocene K-rich volcanism in the southern half of the Sierra Nevada (e.g., Ducea and Saleeby, 1998a; Manley et al., 2000; Farmer et al., 2002). They suggest that delamination may have triggered partial melting in the descending lithospheric mantle, leading to Pliocene volcanism in the southern Sierra, including the Kings River volcanic field. Delamination in the Pliocene, and not in the Miocene, is consistent with the occurrence of lower crustal xenoliths from Sierran volcanic rocks that document the presence of a deep mafic root in the Miocene and its absence in the Pliocene (Ducea and Saleeby, 1996; 1998a,b).

PREVIOUS WORK

The geochemistry, petrography and geochronology of Kings River volcanic suite was first described by Moore and Dodge (1980, 1981), as part of a larger study of both the San Joaquin and Kings River volcanic fields (Fig. 1A), which collectively feature >100 small, glaciated lava flow remnants, several volcanic pipes, and several dikes. Moore and Dodge highlighted the K-rich character of these two volcanic fields. Their K-Ar dates revealed the bimodal Miocene (12-9 Ma) and Pliocene (4-3 Ma) age distribution of the San Joaquin volcanic field and the predominantly Pliocene age (4-3 Ma) of the Kings River volcanic field, which was later confirmed by the addition of 11 $^{40}\text{Ar}/^{39}\text{Ar}$ ages by Manley et al. (2000). With the availability of more precise dates, the Pliocene ages narrowed to mostly 3.4-3.6 Ma. Petrologic studies of the San Joaquin (Van Kooten, 1980) and Kings River (Feldstein and Lange, 1999) volcanic fields pointed out the dominance of phenocrystic olivine ($\leq \text{Fo}_{91}$), as well as the

occurrence of phlogopite \pm leucite in some of the most K-rich flows. These studies presented trace element data that points to an origin of these potassic, Mg-rich lavas in a subduction-modified, lithospheric mantle source. Van Kooten (1981) reported the first $^{87}\text{Sr}/^{86}\text{Sr}$ (0.7060-0.7065) and $^{206}\text{Pb}/^{204}\text{Pb}$ (18.862-19.018) isotopic analyses, with a focus on Pliocene lavas from the San Joaquin volcanic field. Farmer et al. (2002) provides a more comprehensive set of isotopic analyses (Pb, Sr, Nd) of both Miocene and Pliocene lavas from both the San Joaquin and Kings River volcanic field. Their results definitively show that the Pliocene lavas were more potassic, more Mg-rich and had distinctly lower epsilon Nd values (-6 to -8) than adjacent Miocene lavas.

WHOLE-ROCK COMPOSITIONS AND PETROGRAPHY

Methods

The ten Pliocene Kings River samples in this study are a subset of those collected by Feldstein and Lange (1999). These samples were crushed and powdered in a tungsten carbide shatter box at the University of Michigan, and then analyzed for major elements by ICP (inductively coupled plasma) and for trace elements by ICP-MS (mass spectrometry) methods at Activation Laboratories of Ancaster, Ontario, Canada. Whole-rock Ni analyses reported in Table 1 were also performed at Activation Laboratories via single element pressed pellet X-ray fluorescence (XRF). For Ni, the trace element used for olivine-melt thermometry, the XRF detection limit is 1 ppm, and the reproducibility is 4 ppm. (The one exception is PM-3; the Ni content for this sample was obtained by ICP-MS and has a larger error, \pm 20 ppm, than in the other nine samples.) For each sample, a portion of the same rock piece that was powdered for a whole-rock analysis was cut for a thin-section chip for petrography and microprobe analyses.

Results

The whole-rock major-element compositions of the ten Kings River samples used in this study are reported in Table 1, along with select trace element concentrations (Ni, Nb, Zr, Ba, and La). They have compositions that range from 43.8-51.4 wt% SiO₂, 9.4-15.4 wt% MgO, and 1.9-6.6 wt% K₂O. In comparison to the Pliocene Long Valley basalts and Quaternary Big Pine basalts, the Kings River lavas not only extend to higher K₂O and MgO contents, but to lower SiO₂ and Al₂O₃ contents as well (Fig. 2). As noted previously (Feldstein and Lange, 1999; Farmer et al., 2002), chondrite-normalized (McDonough and Sun, 1995) trace-element plots of the Kings River suite show it has an enhanced arc geochemical signature, namely an enrichment in large-ion-lithophile elements relative to high-field strength elements. The enhanced arc signature of the Kings River samples is also seen in the elevated Ba/La ratios (indicative of slab-derived component) that is shared with the Pliocene Long Valley lavas and exceeds those in the Quaternary Big Pine basalts (Fig. 3).

Petrographic examination of the ten Kings River samples from this study shows that the dominant phenocryst in all samples is olivine. It is generally fresh, with little evidence of iddingsite rims. For those samples with the lowest SiO₂ (44-47 wt%) and highest MgO (11-15 wt%), clinopyroxene phenocrysts are either absent or sparse, leading to their classification as basanites in this study. Only three samples (TD-7, TD-10 and BcM-1) contain notable clinopyroxene phenocrysts, which are always subordinate to olivine. Two of these samples (TD-10 and BcM-1) have higher SiO₂ (49-51 wt%) and lower MgO (10-9 wt%) and are classified as trachybasalts. Sparse phlogopite phenocrysts are found in three samples (MP-2, PM-3, and D-1), leading to their classification as minettes. Note that Feldstein and Lange (1999) did not report

phlogopite in MP-2, but it is clearly present in the thin section from this study. Plagioclase is absent as a phenocryst in all samples.

MINERAL COMPOSITIONS AND TEXTURES

Electron Microprobe Analytical Methods

Compositional analyses of olivine and clinopyroxene were obtained using a five-spectrometer Cameca SX-100 electron microprobe at the University of Michigan Robert B. Mitchell Electron Microbeam Analysis Laboratory. The standards used for all analyses are from the University of Michigan collection for the Electron Microprobe (Supplementary Table 1).

Olivine was analyzed in all ten samples in Table 1. Eight elements were analyzed (Mg, Al, Si, Ca, Cr, Mn, Fe, and Ni) using a focused beam with an accelerating voltage of 15 kV and a beam current of 20 nA. Peak counting times were 30 seconds each for Si, Mg, Fe, and Ni, and 20 seconds each for Al, Mn, Cr, and Ca; background counting times were 20 seconds for all eight elements. The counting statistics uncertainty (99% confidence interval) is ± 0.45 wt% SiO₂, ± 0.48 wt% MgO, ± 0.43 wt% FeO, ± 0.05 wt% NiO, ± 0.10 wt% MnO, ± 0.04 wt% for CaO and Al₂O₃, and ± 0.03 wt% for Cr₂O₃.

Between 28 and 83 olivine phenocrysts were analyzed in each thin section (i.e., each sample). Most analyses were conducted along transect lines across individual crystals, with an analysis every 30 to 85 μm . This resulted in five to 30 analyses per olivine and a range of 238-666 analyses per sample. Each transect line was purposefully designed to cross the most Mg-rich part of the olivine crystal (darkest part in a back-scattered electron image) in order to analyze the most Mg-rich olivine composition in each sample.

Clinopyroxene was analyzed in the three samples (BCM-1, TD-7, and TD-10) with clinopyroxene phenocrysts (vs micro-phenocrysts only). Ten elements were analyzed (Mg, Al, Si, Ca, Cr, Mn, Fe, Ni, Na, Ti) utilizing a focused beam with an accelerating voltage of 20 kV and a beam current of 20 nA. For all elements, peak and background counting time of 20 seconds were used. The counting statistics uncertainty (99% confidence interval) is ± 0.47 wt% SiO₂, ± 0.16 wt% MgO, ± 0.12 wt% FeO, ± 0.02 wt% NiO, ± 0.02 wt% MnO, ± 0.28 wt% for CaO, ± 0.10 wt% for Al₂O₃, and ± 0.04 wt% for Cr₂O₃. Most analyses were conducted along transect lines across individual crystals.

Back-scattered electron (BSE) images were obtained for all analyzed olivine and clinopyroxene crystals. In addition, X-ray Wavelength Dispersive Spectrometry (WDS) intensity maps of Fe, P, Ni, Ca, and Mn in the most Mg-rich olivine phenocrysts from three samples (TD-17, MP-2 and PM-3) were acquired using the Cameca SX-100 electron microprobe at the University of Michigan. The maps were collected using an accelerating potential of 20 kV and a beam current of 200 nA, with individual dwell times of 200 μ sec.

Electron Microprobe Results

Olivine

All olivine analyses for each sample are provided in a supplemental file (Supplementary Table 2). Only analyses with totals between 99 and 101 wt% are reported. Histograms of mol% forsterite for each sample (Fig. 4) show a continuous range of composition, with no evidence of bimodality (i.e., magma mixing). For the basanite samples, the olivine phenocrysts span a range of 5-10 mol% Fo content, whereas for the three minette samples (MP-2, PM-3 and D-1), they span a narrower compositional range (≤ 5 mol% Fo).

The most Mg-rich olivine composition in each sample is reported in Table 2. Plots of analyzed MnO (wt%), NiO (wt%) and CaO (wt%) versus mol% forsterite are shown for all samples (Figs. 5, 6 and 7). For all three trace elements, a linear fit to their concentrations in the highest three mol% forsterite olivine was obtained for each sample. The one exception is for sample PM-3 where a linear fit to only the highest 1 mol% Fo olivine is made for MnO, NiO and CaO is required. The linear fit enables a more accurate mean concentration to be calculated in the most Mg-rich olivine, which is reported in Table 3.

X-ray intensity maps of Fe, P, Mn, Ni and Ca are shown for the most Mg-rich olivine crystal analyzed in three representative samples from this study, MP-2, TD-17, and PM-3, in Figures 8 and 9. The results show that the complex zoning patterns for P are distinctly different than that for Fe in three of four olivine phenocrysts. Among the bivalent trace elements, Ni displays the strongest zonation in all olivine crystals from all three samples, which reflects the relatively high partition coefficient between Ni and melt (Table 2). Ca is slightly enriched along a thin rim in the olivine crystals from the two minette samples, whereas Ca displays no zonation in the olivine from TD-17. Mn is only weakly zoned in the two olivine crystals from minette PM-3, but it displays rim enrichments in olivine in TD-17 and especially MP-2. BSE images of representative olivine phenocrysts are shown in Fig. 10. Many of the olivine phenocrysts in the Kings River basanites and minettes display diffusion-limited growth textures (i.e., dendritic and hopper).

Clinopyroxene

All clinopyroxene phenocryst analyses (in each of the three samples where they were found; TD-7, TD-10 and BcM-1) are provided in a supplemental file (Supplementary Table 3).

Again, only analyses with 99-101 wt% totals are reported. Histograms of Mg# for each sample are shown in Fig 11, and they are compared to the Mg# histogram of olivine analyzed in the same samples. Note that in all three samples, the maximum Mg# of clinopyroxene exceeds or is equal to that of the maximum Mg# (mol% Fo) of olivine. The most Mg-rich clinopyroxene analyzed in each sample is reported in Table 3. BSE images of the most Mg-rich clinopyroxene analyzed in each of these three samples are shown in Figure 12. Note the occurrence of Mg-rich clinopyroxene as large mineral inclusions in olivine in one of these samples (BcM-1), which is consistent with clinopyroxene rather than olivine as the possible liquidus phase.

TEST OF PHENOCRYST GROWTH DURING ASCENT

Evidence of diffusion-limited growth textures

There is strong evidence that many primitive basalts, especially those that entrain mantle xenoliths, may have transited the crust rapidly along dikes, without stalling in crustal magma chambers (e.g., Brehm and Lange, 2020). Although none of the ten Kings River samples from this study entrained mantle xenoliths, several Pliocene flows from the San Joaquin volcanic field did (e.g., Van Kooten, 1981; Ducea, 1996). This points to rapid transit of these mantle-derived melts through the crust and precludes their storage in crustal chambers prior to eruption. Otherwise, the entrained mantle xenoliths would have dropped out and not been carried to the surface. In these cases, any phenocrysts that grew in these melts must have grown rapidly, during ascent along fractures over a period of days, and are expected to display diffusion-limited growth textures.

Many of the olivine phenocrysts in the Kings River samples have features indicative of rapid growth, including dendritic and/or hopper textures (Fig. 10). Such diffusion-limited growth

textures are expected for melts undergoing crystallization during an effective undercooling ($\Delta T_{\text{eff_uc}} = T_{\text{liquidus}} - T_{\text{melt}}$) (e.g., Shea et al., 2019). For hydrous basalts that initially segregate from their mantle source under fluid undersaturated conditions, initial ascent will lead to super-liquidus conditions because their liquidus temperatures will decrease with decreasing pressure. During continued ascent along fractures, the effects of cooling, and eventually volatile degassing, will lead these basalts to cross their liquidus, but from a super-liquidus condition (e.g., Brehm and Lange, 2020). This will promote a kinetic delay to nucleation, allowing an effective undercooling to develop, which enables the growth of large phenocrysts, owing to high crystal growth rates and low nucleation rates (e.g., Lofgren, 1974).

A test of whether the most Mg-rich olivine (or clinopyroxene) in each sample was the liquidus phase for the whole-rock melt composition

A test of whether the Kings River samples from this study ascended rapidly to the surface and grew their phenocrysts in route to the surface along dikes can be made by evaluating whether the most Mg-rich olivine (or clinopyroxene) in each sample represents the equilibrium liquidus composition expected for a melt with the whole-rock composition. In other words, if phenocryst growth during ascent was sufficiently rapid, such that there was insufficient time for diffusive re-equilibration of the liquidus olivine composition, it is possible that it may be preserved and its composition captured during analyses of olivine in thin section (e.g., Fig. 4). Conversely, if transit to the surface was slow and diffusive re-equilibration of the liquidus olivine composition occurred, equilibrium tests can be deployed to identify those cases.

To test the hypothesis of whether the most Mg-rich analyzed olivine has a composition expected under equilibrium conditions at the liquidus, equilibrium tests were applied to the most

Mg-rich olivine analyzed in each sample paired with the whole rock (liquid) composition. One test is based on the Fe²⁺-Mg exchange reaction between olivine and melt, whereas the other is based on the Mn-Mg exchange reaction. For any clinopyroxene-bearing samples that fail the olivine-liquidus test, a Fe^T-Mg K_D test of whether the most Mg-rich clinopyroxene is the plausible liquidus phase is made in the section on clinopyroxene-melt barometry.

Fe²⁺-Mg K_D olivine-melt equilibrium test at the liquidus

The Fe²⁺-Mg exchange partition coefficient is defined by the following reaction:

$${}^{\text{Fe}^{2+}\text{-Mg}}K_D (\text{oliv-melt}) = (X_{\text{FeO}}/X_{\text{MgO}})^{\text{olivine}} / (X_{\text{FeO}}/X_{\text{MgO}})^{\text{melt}} \quad (1)$$

where X_{MgO} and X_{FeO} refers to the mole fraction of ferrous iron and magnesium oxide, respectively, in olivine and melt. Although all iron in olivine is ferrous, this is not the case for the melt phase; melt ferric-ferrous ratios must be known to calculate ^{Fe²⁺-Mg}K_D (oliv-melt) values. Since there is no independent means to assess the oxidation state in the Kings River melts (e.g., Fe-Ti oxybarometry) at the onset of their phenocryst growth, an initial estimate for the Fe³⁺/Fe^T ratio of 0.20 (equivalent to ΔNNO = -0.4) was employed.

With an Fe³⁺/Fe^T ratio of 0.20 applied to each the whole-rock composition of all ten Kings River samples, equation 1 can be used to calculate the ^{Fe²⁺-Mg}K_D (oliv-melt) value when the most Mg-rich olivine in each sample is paired with its whole-rock liquid composition. The resulting ^{Fe²⁺-Mg}K_D values are tabulated in Table 4a and range from 0.25 to 0.35 for seven of eleven samples; six of these seven are within ≤ 0.03 of the ^{Fe²⁺-Mg}K_D values predicted from models in the literature, including the MELTS thermodynamic model (Ghiorso and Sack, 1995; Asimow and Ghiorso, 1998) and Putirka (2016; equation 8c). Because the Putirka (2016) model is used to calculate ferric-ferrous ratios, for internal consistency that study's experimentally

calibrated model is used to calculate $^{Fe^{2+}-Mg}K_D$ (olivine-melt) for a comparison with our measured values for the ten Kings River samples (Table 4a).

As seen in Figure 4a, there are three samples (TD-12, TD-7 and BcM-1) that have apparent $^{Fe^{2+}-Mg}K_D$ olivine-melt values that range from 0.40-0.55, which deviate strongly from predicted values ($\sim 0.32 \pm 0.03$) and would require that nearly all of the iron in these samples is ferrous (i.e., highly reduced). It is perhaps not surprising that two of these three samples (TD-7 and BcM-1) contain clinopyroxene phenocrysts that span a higher range of Mg# than their coexisting olivine phenocrysts (Fig. 11), which strongly indicates that clinopyroxene (and not olivine) is the likely liquidus phase in these two samples. With respect to the third sample, TD-12, it is possible that olivine underwent partial diffusive re-equilibration, such that the most Mg-rich olivine that initially grew from this melt at the liquidus is no longer preserved. Alternatively, it may have undergone olivine accumulation, which might also explain the notably high MgO content of this sample (15.4 wt%).

For sample TD-8, which has a relatively low $^{Fe^{2+}-Mg}K_D$ olivine-melt value of 0.25 that deviates by 0.06 from that predicted for this melt composition using the Putrika (2016) model, it is possible that it was slightly more oxidized than the other samples, on average. If TD-8 is assigned a melt Fe^{3+}/Fe^T ratio of 0.30 (equivalent to $\Delta NNO = +0.8$), instead of the initially assumed value of ~ 0.20 (equivalent to $\Delta NNO = -0.4$), it passes the $^{Fe^{2+}-Mg}K_D$ olivine-melt test. These results underscore the need to apply an alternative exchange reaction between olivine and melt that does not depend on the melt ferric-ferrous ratio. Blundy et al. (2020) experimentally calibrated a lattice strain model for $^{Mn-Mg}K_D$ (oliv-melt) that is independent of melt composition, including the ferric-ferrous ratio. However, because this model requires that temperature (and

olivine composition) be known, this test is applied in a later section after olivine-melt thermometry is performed.

OLIVINE-MELT THERMOMETRY

As discussed above, seven of the ten Kings River samples in this study pass the $^{Fe^{2+}-Mg}K_D$ (olivine-melt) equilibrium test at $Fe^{3+}/Fe^T = 0.20-0.30$. This supports the hypothesis that olivine-melt thermometry can be applied at the liquidus of those samples by pairing the most Mg-rich olivine in each sample (Table 3) with a liquid that has the whole-rock composition to obtain the temperature at the onset of phenocryst growth. We employed the Mg- and Ni-based thermometer of Pu et al. (2017), which were calibrated on the same experimental data set. Note that the melt and olivine compositions in the Kings River samples (Tables 1 and 2) fall within the range of compositions used to calibrate the two thermometers (Pu et al., 2017, 2021). Values of molar $D_{Mg}^{ol/liq}$ and $D_{Ni}^{ol/liq}$ were constructed for each of the Kings River samples using the MgO and Ni contents in the most Mg-rich olivine composition (Table 2) paired with their respective MgO and Ni contents in the whole-rock composition (Table 1). When the values of $D_{Mg}^{ol/liq}$ are input into the Mg-based thermometer of Pu et al. (2017), resulting temperatures range from 1257-1368 °C and increase linearly with whole-rock MgO content (9.4-15.4 wt%; Fig. 13). These temperatures are within 3 degrees, on average, of those calculated using the Mg-based olivine-melt thermometer of Putirka et al. (2007) without a correction for H₂O. Analytical uncertainties due to microprobe and whole-rock analyses lead to relative errors of ±1-2% for $D_{Mg}^{ol/liq}$, which propagate to uncertainties in T_{Mg} of ±4-6°C.

Given the presence of phlogopite in some of the Kings River samples, it is expected that dissolved water was present in these melts at the onset of olivine crystallization. Therefore, it is

expected that temperatures based on the Mg-thermometer are too high (i.e., reflect anhydrous conditions). In fact, when the values of $D_{\text{Ni}}^{\text{ol/liq}}$ are input into the Ni-based thermometer of Pu et al. (2017), resulting temperatures are significantly lower and range from 1023 to 1224 °C (Table 4; Fig. 13). These reflect the actual temperature at the onset of olivine crystallization in these samples.

Analytical uncertainties due to microprobe and whole-rock analyses lead to relative errors of $\pm 3\text{-}6\%$ for $D_{\text{Ni}}^{\text{ol/liq}}$, which propagate to uncertainties in T_{Ni} of $\pm 6\text{-}12^\circ\text{C}$. Note that the sample with the lowest Ni content (TD-10; 149 ppm) has the largest error in T_{Ni} ($\pm 12^\circ\text{C}$), whereas those >200 ppm Ni have lower T_{Ni} errors ($\leq \pm 9^\circ\text{C}$). This result underscores the utility of working with samples with high whole-rock (i.e., liquid) Ni concentrations to obtain relatively low uncertainties in T_{Ni} values.

The $^{\text{Mn-Mg}}K_{\text{D}}$ olivine-melt equilibrium liquidus test

The $^{\text{Fe}^{2+}\text{Mg}}K_{\text{D}}$ olivine-melt liquidus test applied above depends on an independent constraint on melt oxidation state, which is not known and can only be estimated. It is therefore necessary to apply an alternative equilibrium test to the Kings River samples that is independent of melt oxidation state, namely the equilibrium exchange of Mn and Mg between olivine and melt. Blundy et al. (2020) provides an experimentally calibrated, lattice strain model that allows $^{\text{Mn-Mg}}K_{\text{D}}$ olivine-melt values to be calculated based only on temperature and olivine composition. The advantage of this test is that it is independent of melt composition, including ferric-ferrous ratio and dissolved H_2O content, and it is only weakly dependent on temperature (e.g., a change of 50°C only changes the $^{\text{Mn-Mg}}K_{\text{D}}$ value by ~ 0.01).

When the T_{Ni} values obtained for the Kings River samples are respectively combined with their most Mg-rich olivine composition (Table 2), the resulting $^{Mn-Mg}K_D$ values calculated with the Blundy et al. (2020) lattice strain model range from 0.18-0.22 (± 0.03). For eight of ten samples, these values are within ≤ 0.04 of those measured in this study (Table 4b), based on whole-rock and olivine MnO and MgO concentrations (Fig. 5; Tables 1 and 2), and thus pass the $^{Mn-Mg}K_D$ olivine-melt liquidus test.

Among the eight samples that pass the $^{Mn-Mg}K_D$ olivine-melt liquidus test is TD-8, which confirms that it likely had a slightly higher oxidation state relative to most of the other Kings River samples (in order to pass the $^{Fe^{2+}-Mg}K_D$ olivine liquidus test). Interestingly, TD-12 also passes the $^{Mn-Mg}K_D$ olivine-melt liquidus test, with no difference between the measured (this study) and calculated (Blundy et al., 2020) values (Table 4b), despite failing the $^{Fe^{2+}-Mg}K_D$ olivine-melt test. This raises the possibility that it may have been reduced relative to the other Kings River samples.

There are two samples (TD-7 and BcM-1), however, that clearly fail the $^{Mn-Mg}K_D$ olivine liquidus test, with notably large deviations of 0.13 and 0.32, respectively (Table 4b). Note that these two samples also clearly failed the $^{Fe^{2+}-Mg}K_D$ olivine liquidus test (Table 4a), and they are the two samples with clinopyroxene phenocrysts with higher Mg# values than coexisting olivine phenocrysts (Fig. 11). The hypothesis of whether clinopyroxene was the liquidus phase in these two samples can be tested using the $^{Fe^{T}-Mg}K_D$ clinopyroxene-melt equilibrium test. If so, then the clinopyroxene-melt thermometer and barometer of Neave and Putirka (2017) can be applied to these samples.

CLINOPYROXENE-MELT BAROMETRY

Evidence that clinopyroxene is the liquidus phase in three samples

In addition to the two samples (TD-7 and BcM-1) that failed both olivine liquidus tests, there is a third sample (TD-10) that also contains clinopyroxene phenocrysts. When the most Mg-rich clinopyroxene analyzed in each of these three samples is paired with the respective whole-rock composition, the resulting $^{FeT-Mg}K_D$ values (0.29, 0.25, 0.26, respectively) overlap the range predicted for clinopyroxene-liquid Fe-Mg exchange equilibrium (0.27 ± 0.03 ; Putirka, 2008). These results support the hypothesis that clinopyroxene was the liquidus phase in each of these three samples.

Note that the most Mg-rich olivine analyzed in TD-10 also passes the $^{Fe^{2+}-Mg}K_D$ and $^{Mn-Mg}K_D$ equilibrium tests for being the liquidus phase (Table 3a), and it is likely that both olivine and clinopyroxene were co-saturated on the liquidus in this sample. In contrast, clinopyroxene was the sole liquidus phase in both TD-7 and BcM-1. For all three samples, clinopyroxene-melt barometry can be applied at the liquidus.

Depth at the onset of clinopyroxene growth

The clinopyroxene-melt barometer of Putirka and Neave (2017) was applied to samples TD-7, TD-10, and BcM-1 to calculate the pressure (depth) at the onset of phenocryst growth. In each case, the most Mg-rich clinopyroxene (Table 5) was paired with a melt that matches the whole-rock composition. For samples TD-7 and BcM-1, both temperature (1208 and 1188 °C, respectively) and pressure (0.53 and 0.51 GPa) were calculated since the olivine-melt thermometer cannot be applied. For sample TD-10, temperature is known independently from the Ni-based olivine-melt thermometer (Table 4), given the evidence that both olivine and clinopyroxene were co-saturated on the liquidus. At this temperature ($T_{Ni} = 1047$ °C), the

Putirka and Neave (2017) barometer calculates a pressure of 0.5 GPa for the onset of clinopyroxene (and olivine) phenocryst growth. Thus, for all three samples, it appears that the onset of crystallization occurred at depths of ~19-20 km (Table 5).

OLIVINE-MELT HYGROMETRY

The thermometry results in Fig. 13 show that the temperatures based on $D_{Mg}^{ol/liq}$ (T_{Mg}) are consistently higher than those based on $D_{Ni}^{ol/liq}$ (T_{Ni}). The large difference between the two temperatures, namely $\Delta T = T_{Mg} - T_{Ni}$, is a measure of how much the olivine liquidus temperature was depressed because of dissolved H₂O in the melt phase. For the eight Kings River samples for which olivine-melt thermometry could be applied, the ΔT values range from 129-299°C (Table 4). The average ΔT value among all ten samples is 201°C. Note that if the highest ΔT of 299°C (for PM-3, for which Ni content not yet analyzed by XRF method) is not included, the ΔT values range from 129-234°C, with an average of 186 °C.

These ΔT values can be converted to dissolved melt H₂O contents using the updated calibration from Pu et al. (2023). In that study, an evaluation of 35 hydrous olivine-melt equilibrium experiments from the literature (Sisson & Grove, 1993a,b; Wagner et al., 1995; Righter & Carmichael, 1996; Moore & Carmichael, 1998; Berndt et al., 2005; Almeev et al., 2007; Médard & Grove, 2008; Parman et al., 2011) under near-liquidus conditions (≤ 5 % olivine) was performed. The final data set spans a wide range of olivine composition (Fo78-95) and melt composition (47-58 wt% SiO₂; 4.4-10.2 wt% MgO; 1.3-4.9 wt% Na₂O; 0.1-5.0 wt% K₂O; 0.3-5.3 wt% H₂O). Experimental temperatures range from 1024-1220 °C, whereas pressures range from 0.001 to 0.2 GPa. Pu et al. (2023) show that the relationship between wt % dissolved water in the melt and ΔT (i.e., the depression of the olivine liquidus temperature due to

water) is linear, with no dependence on melt composition ($\text{wt\% H}_2\text{O} = 0.047 \cdot \Delta T$). When this relationship is applied to the Kings River samples, the resulting water contents at the onset of olivine crystallization range from 6-14 wt%, with an average value of 9.4 wt% H_2O (Table 4). Again, if PM-3 is not included (which may be an outlier since the Ni analysis for this sample was not the more accurate XRF method; Table 1), the resulting water contents range from 6-11 wt%, with an average value of 8.8 wt%. An additional caveat is that most of the ΔT and wt% H_2O values obtained for the Kings River suite are larger than those used in the Pu et al. (2023) experimental calibration (≤ 130 °C and ≤ 6 wt%).

Another assessment of melt water contents can be made through application of the Putirka et al. (2007) Mg-based olivine-melt thermometer, which includes a correction for H_2O content in the melt. When an H_2O correction is not made, the Putirka et al. (2007) Mg-thermometer gives anhydrous temperatures for the Kings River samples that are within ± 5 °C of those calculated with the Pu et al. (2017) Mg-thermometer. When wt% H_2O is input into the Putirka et al. (2007), with the goal of obtaining temperatures that match those from the Ni-thermometer, the resulting water contents are similar to those obtained using the updated calibration of Pu et al. (2023). The average H_2O content among all samples is 8.6 wt% (excluding PM-3), which is close to the average of 8.8 wt% obtained from the Pu et al. (2023) model. Individual differences between the two models range from -1.0 to 0.7 wt% H_2O , with an average difference of -0.1 wt% (Table 4). Although both models give similar results, for reasons of internal consistency, we recommend use of the Pu et al. (2023) calibration to calculate wt% H_2O when applied to $\Delta T (=T_{\text{Mg}} - T_{\text{Ni}})$ values obtained with the Pu et al. (2017) Mg- and Ni-thermometers.

Effect of pressure correction on H₂O calculations

Given the clinopyroxene-melt barometry results, it is likely that the onset of phenocryst growth in the Kings River samples occurred at depth, which raises the question of what is the effect of applying pressure corrections to T_{Mg} and T_{Ni} , which will impact $\Delta T (=T_{Mg}-T_{Ni})$ and thus hygrometry results. If an average pressure correction at 0.5 GPa is applied, this will increase all T_{Mg} values by 27 degrees (using the correction of Herzberg and O'Hara, 2002) and all T_{Ni} values by 11 degrees (using the correction of Pu et al., 2023; equation 2), as indicated in Table 4. Thus, all ΔT results calculated at 0.5 GPa will be ~ 16 °C larger than those calculated without any pressure correction (Table 4). This increase leads to an increase of ~ 0.7 wt% in the average melt H₂O content (from 8.8 to 9.5 wt% H₂O) calculated from the Pu et al. (2017; 2023) hygrometer for all Kings River samples (excluding PM-3). The main conclusion, therefore, is that olivine-melt hygrometry results that do not include a pressure correction are minimum estimates. For a pressure correction at 0.5 GPa, they are too low by ~ 0.7 wt% H₂O.

Relationship between ΔT (wt% H₂O in melt) and $\ln D_{Ca}^{ol/liq}$

Confirmation that the large $\Delta T (=T_{Mg}-T_{Ni})$ values obtained for the Kings River samples reflect high H₂O contents in the melt phase is found by plotting their ΔT values (both for individual samples and the average for the volcanic field) against $\ln D_{Ca}^{ol/liq}$ values from Table 2 (Fig. 14). It has been previously noted in the literature (e.g., Gavrilenko et al., 2016) that the CaO content in olivine is sensitive to dissolved H₂O contents in the coexisting melt phase.

In Fig. 14a-b, we compare the average $\Delta T (=T_{Mg}-T_{Ni})$ and average wt% H₂O against the average $\ln D_{Ca}^{ol/liq}$ values obtained for seven different volcanic fields where the Pu et al. (2017) olivine-melt thermometer/hygrometer has been applied: (1) the Kings River volcanic suite from

this study; (2) the Colima cone suite in the Mexican arc (Pu et al., 2023), (3) the calc-alkaline Tancítaro volcanic field (TVF) in the Mexican arc (Pu et al., 2017), (4) the Long Valley, CA basalts (Jolles & Lange, 2021), (5) the Big Pine, CA basalts (Brehm & Lange, 2020), (6) the Yellowstone and Snake River Plain basalts (Brehm, 2021), and (7) the mid-ocean ridge basalt (MORB) suite from Allan et al. (1989) studied by Pu et al. (2017). There is a strong, inverse linear correlation ($R^2=0.992$) where the largest (i.e., least negative) $\ln D_{Ca}^{ol/liq}$ average (-3.79) is found in the MORB suite, which are nearly anhydrous (~0.1 wt% H₂O), whereas the volcanic field with the lowest (i.e., most negative) average $\ln D_{Ca}^{ol/liq}$ value (-4.50) is the Kings River volcanic suite from this study.

Note that the volcanic field with the next highest average ΔT value (and most negative $\ln D_{Ca}^{ol/liq}$ average) relative to the Kings River volcanic field is the Colima cone suite, in the Mexican arc (Pu et al., 2023). The Colima cone lavas are very similar to those in the Kings River suite and include high-MgO (9-13 wt%) basanites and minettes with an enhanced arc geochemical signature. The average wt% H₂O content for the Colima cone suite is 6.2 wt% H₂O, which is close to the highest analyzed H₂O content directly analyzed in olivine-hosted melt inclusions (≤ 7.0 wt% H₂O; Vigouroux et al., 2008; Maria & Luhr, 2008).

The Tancítaro volcanic field (TVF) has the next highest average ΔT (113°C) and lowest $\ln D_{Ca}^{ol/liq}$ value (-4.44), and is also from the Mexican arc (Pu et al., 2017). This ΔT value converts to an average wt% H₂O of 5.2 wt%, which is close to the highest analyzed H₂O content directly analyzed in olivine-hosted melt inclusions (≤ 5.7 wt% H₂O; Johnson et al., 2009). The remaining volcanic field for which direct H₂O analyses in olivine-hosted melt inclusions are available is the Big Pine, CA volcanic field (≤ 3.0 wt% H₂O; Gazel et al., 2012), which has an average calculated value of 2.8 wt% H₂O obtained from olivine-melt hygrometry (Fig. 14b;

Brehm and Lange, 2020). Thus, in each of the three volcanic fields where there are direct analyses of H₂O from olivine-hosted melt inclusions, there is strong agreement with results obtained with the olivine-melt hygrometer of Pu et al. (2017).

In Figure 14a and 14b, the ΔT and wt% H₂O results for individual samples from the Kings River suite are also plotted against their respective $\ln D_{Ca}^{ol/liq}$ values. Although there is scatter around the average, the samples broadly plot along the inverse linear array defined by the averages of all the volcanic fields. In other words, the sample with the lowest ΔT value (TD-4) also has the highest (least negative) $\ln D_{Ca}^{ol/liq}$ value, whereas those samples with the highest ΔT values have some of the lowest (most negative) $\ln D_{Ca}^{ol/liq}$ values. Collectively, the results in Figure 14 strongly support the finding that the Kings River suite of basanites and minettes are among the most hydrous mantle-derived melts that have been documented to date.

DISCUSSION

Comparison of Kings River basanites/minettes to Long Valley and Big Pine basalts

Differences in temperatures and melt H₂O contents

One of the key questions addressed in this study is whether there was a significant difference in the temperature and/or H₂O content of the Kings River basanites and minettes relative to the Long Valley and Big Pine basalts to explain the much higher MgO contents of the former. In the plot of T_{Mg} and T_{Ni} vs. wt% MgO (Fig. 13), a comparison between the Kings River and Long Valley/Big Pine samples at a common MgO content (~10 wt%) shows that the Kings River sample had much lower temperatures and thus higher melt H₂O contents.

It is perhaps more revealing to compare the two suites in a plot of wt% H₂O in the melt vs. temperature (at onset of olivine crystallization; Fig. 15). The results fall on two distinct trend

lines with the Kings River samples on one, and both the Long Valley and Big Pine basalts overlapping on the other. Each trend line (i.e., linear fit; Fig. 15) shows that as H₂O content increases, the temperature at the onset of olivine crystallization decreases. Note that there is no difference in the range of temperatures between the Kings River suite and the Long Valley and Big Pine basalts (in fact, the Kings River samples are shifted to slightly lower temperatures). Instead, the Kings River basanites and minettes are notable for their much higher H₂O contents at a similar melt temperature (e.g., ~5 wt% higher at 1150°C; Fig. 15). The fact that there are two distinct trend lines in Figure 15 raises the question of whether the Kings River basanite and minette melts were derived from a distinctly different (i.e., more refractory) mantle source compared to those that led to the formation of the Long Valley and Big Pine basalts.

Differences in melt segregation depths

Evidence of different mantle sources is consistent with evidence that the Kings River suite segregated from its mantle source at greater depths than the Long Valley and Big Pine basalts. For example, results from two experimental studies on the partial melting of phlogopite-bearing lherzolite and harzburgite at 1 and 3 GPa (Condamine & Medard, 2014; Condamine et al., 2016) can be used to constrain the pressure of mantle melt segregation for the Kings River samples. Plots of the concentration of MgO and Al₂O₃ vs SiO₂ in the experimental melts show a strong pressure dependence (Fig. 16), with higher pressures favoring higher MgO and lower Al₂O₃ and SiO₂ contents. The Kings River samples plot on either side of the 3 GPa experimental melts, leading to an estimated average melt segregation pressure of ~2.5-3.0 GPa (~80-100 km). In contrast, the Long Valley basalts have compositions that plot closer to ~1 GPa (vs 3 GPa) experimental melts, leading to an estimated average melt segregation pressure of ~1.5-2.0 GPa

(~50-60 km). These estimates are consistent with trace element constraints (i.e., Sm/Yb ratios) that point to a garnet- vs spinel-bearing mantle source for the Pliocene southern Sierran lavas (which includes the Kings River volcanic field) vs the Long Valley basalts, respectively (e.g., Putirka et al., 2012). Previous studies have also confirmed that the Big Pine basalts were segregated from spinel-bearing mantle at depths that overlaps those inferred for the Long Valley basalts (e.g., Gazel et al., 2012; Putirka et al., 2012).

A possible difference in mantle source region?

Previous studies from the literature present Sr and Nd isotopic analyses that show the Long Valley and Big Pine volcanic fields have overlapping isotopic compositions, indicative of their derivation from an isotopically similar mantle source (e.g., whole rock $^{87}\text{Sr}/^{86}\text{Sr}$ ratios range from 0.7053 to 0.7067, and epsilon Nd values ranges from -6.0 to 0; Ormerod et al., 1991; Beard and Glazner, 1995; Cousens, 1996). In contrast, data from Farmer et al. (2002) show that most of the Kings River volcanic suite is shifted to higher whole-rock $^{87}\text{Sr}/^{86}\text{Sr}$ ratios (0.7064-0.7072) and lower epsilon Nd values (-8.0 to -6.0), indicative of a distinctly different lithospheric mantle source that is Proterozoic in age. Most researchers agree that subduction-modified, continental mantle lithosphere (CML), and not asthenosphere, is the source for all three volcanic fields, but an emerging question is whether there are two distinctly different CML beneath these three volcanic fields as suggested by Farmer et al. (2002). In contrast, Putirka et al. (2012) propose that there is only one CML, which is the mantle source for the Pliocene San Joaquin and Kings River volcanic suites. They further argue that this same Proterozoic CML exists further to the east beneath the Long Valley and Big Pine volcanic fields, but that here it has been infiltrated and degraded by partial melts of upwelling asthenosphere, which not only explains the shifted

isotopic compositions of the Long Valley and Big Pine basalts relative to the Kings River basanites and minettes, but also why their mantle source is more fertile. Putirka et al. (2012) thus propose that delamination of Proterozoic CML brought it down to depths of ~80-120 km beneath the Kings River volcanic field, leading to the formation of partial melts in the garnet stability field, which erupted to form the Pliocene San Joaquin and Kings River volcanic fields. In contrast, they propose that to the east, beneath the Long Valley and Big Pine volcanic fields, the Proterozoic CML was thinned and variably infiltrated by asthenospheric partial melts, leading to partial melts of this thinned mantle in the spinel stability field. The Putirka et al. (2012) model explains the whole-rock major- and trace-element compositions of all three volcanic fields (driven, in part, by differences in their melt segregation depths from their respective mantle sources), as well as their differences in isotopic compositions. What it does not explain, however, is what was the source of the unusually high-water contents in the Kings River basanites and minettes.

What was the source of H₂O for the unusually hydrous Kings River suite?

Owing to the absence of active subduction beneath the southern Sierra Nevada during the Pliocene, the release of an H₂O-rich fluid phase from subducting oceanic lithosphere cannot be called upon as the source of H₂O in the Kings River basanites and minettes. Therefore, an outstanding question is what was the source of the extraordinarily high concentrations of water in the Kings River magmas (Table 4; Figure 14b)?

Prior to this study, it had been assumed that any dissolved water in the Kings River basanites and minettes must have originated from the melting of phlogopite in the mantle source (e.g., Feldstein and Lange, 1999; Elkins-Tanton and Grove, 2003). However, it is not possible to

form melts with >5 wt% H₂O (and <4 wt% K₂O) if the sole source of H₂O is phlogopite in the mantle source. This point was made by Vigouroux et al. (2008), where they used the experimental data of Esperanca and Holloway (1987) to derive a stoichiometry for the melting reaction in phlogopite-bearing mantle, where ~0.51 g of phlogopite reacts to form ~1.1 g of melt. Since phlogopite contains <4-5 wt% H₂O (e.g., Sweeney et al., 1993; Haggerty, 1995; Righter et al., 2002), the resulting melt can only contain approximately half (i.e., $\sim 0.51/1.1 = 46\%$) of this amount (<1.9-2.3 wt% H₂O). However, Pu et al. (2023) point out that in the more recent experiments of Condamine et al. (2016), the proportion of phlogopite in the melting reaction is shown to increase strongly in a depleted harzburgitic mantle (~0.96 g of phlogopite reacts to form ~1.0 g of melt) relative to a more fertile lherzolite mantle (~0.59 g of phlogopite reacts to form ~1.0 g of melt). Thus, for a phlogopite-bearing harzburgitic mantle, nearly 96% of the H₂O in phlogopite will be contained in the melt. But even in this case, not only is there an upper limit of ~5 wt% H₂O in the partial melt, but the melt is also expected to contain >4-6 wt% K₂O, due to the significant involvement of phlogopite in the melting reaction (as seen in the experimental melts of Condamine et al., 2016). What is so unusual about the Kings River samples, therefore, is not only are these melts unusually hydrous (~6-11 wt% H₂O; Table 4), but they are also only moderately potassic (~1.9-4.4 wt% K₂O in all but one case; Table 1). Thus, the source of their elevated H₂O concentrations cannot lie solely with phlogopite in their mantle source region.

Here, it is hypothesized that the location of the Kings River volcanic field on top of the lithospheric boundary between accreted oceanic lithosphere (Panthalassa) and Proterozoic North America (e.g., Kistler, 1990; Ducea, 2001; Saleeby, 2011) is key to understanding the source of their unusually high H₂O concentrations. Although the isotopic study of Farmer et al. (2002) clearly shows that Proterozoic North American lithosphere is the mantle source of the Kings

River volcanic suite, it is highly probable that it was in close contact with thrust slices of serpentinitized mantle from the Panthalassan lithosphere (Fig 1a).

Here, it is proposed that during delamination of the Proterozoic North American continental mantle lithosphere (CML), there were slices of serpentinitized mantle embedded in (or adjacent to) the Proterozoic CML. As the lithosphere beneath the Kings River volcanic field underwent delamination, it gradually began to heat up due to contact with deeper asthenosphere. With gradually increasing temperatures, the first reaction would have been dehydration of serpentine, releasing H₂O fluid from regions of serpentinitized mantle. Experimental studies show that serpentine dehydrates at relatively low temperatures (≤ 700 °C) at 2-3 GPa (e.g., Ulmer and Trommsdorff, 1995), in contrast to phlogopite, which does not dehydrate, but instead melts at >1200 °C at these pressures (e.g., Condamine et al., 2014, 2016). Moreover, the breakdown of serpentine releases ~13 wt% H₂O versus a maximum of ~5 wt% H₂O from phlogopite. Thus, it appears that the occurrence of the unusually high concentrations of H₂O in the Kings River volcanic suite may owe its origin to its unique tectonic setting on top of the boundary between Panthalassan oceanic lithosphere and North American continental lithosphere.

CONCLUSIONS AND IMPLICATIONS

Several key conclusions can be drawn from this study of the Pliocene Kings River volcanic suite, which erupted through the southern Sierra Nevada granitoid batholith. First and foremost, the unusually high MgO contents (9-15 wt%) of these basanite, minette and trachybasalt samples reflect liquid compositions. For all ten samples, either the most Mg-rich olivine or clinopyroxene passes equilibrium tests for being the first phenocryst to crystallize from the melt during ascent. The eruption of such Mg-rich liquids, without undergoing significant

differentiation, is consistent with rapid ascent via fractures from their mantle source region. The fact that similar Pliocene lavas to the north (San Joaquin volcanic field) entrain mantle xenoliths supports the hypothesis that these Mg-rich melts transited rapidly through the crust, without stalling in crustal magma chambers prior to eruption. The olivine phenocrysts in all samples display evidence of rapid-growth textures, consistent with degassing-induced crystallization during ascent. Application of clinopyroxene-melt barometry (Neave and Putirka, 2017) to three samples shows the onset of phenocryst growth occurred at ~0.5 GPa (~20 km).

Second, application of Mg- and Ni-based olivine-melt thermometers (Pu et al., 2017) provides both the temperature and the H₂O content in the eight samples with olivine on the liquidus. The Ni-based thermometer is independent of dissolved H₂O in the melt and gives temperatures (T_{Ni}) that range from ~1220 to 1047 °C, with an average uncertainty of ± 8 °C, for melts that range from 15.4 to 10.2 wt% MgO. When combined with the Mg-based thermometer, which gives the anhydrous temperature (T_{Mg}), the depression of the olivine liquidus due to dissolved H₂O content in the melt ($\Delta T = T_{Mg} - T_{Ni}$) was shown to range from 234-129 degrees, with an average ΔT of 186 degrees. Corrections for the effect of pressure (i.e., evidence that phenocryst growth began at ~0.5 GPa), increase ΔT by ~16°C. Application of an updated calibration that relates the magnitude of the depression of the olivine liquidus (i.e., ΔT) with dissolved H₂O in the melt (Pu et al., 2023), leads to calculated water contents for the Kings River suite that range from 6.1-11.0 wt%, with an average of 8.8 wt% H₂O.

Third, a comparison of calculated temperatures and dissolved wt% H₂O in the melt (at the onset of olivine phenocryst growth) between the Kings River suite and both the Long Valley and Big Pine basalts (erupted along the eastern escarpment of the Sierra Nevada) show two distinct trend lines. Samples from the Kings River suite fall along a linear trend that is shifted to

higher H₂O contents (by ~5 wt%) at a given temperature compared to the samples from the Long Valley and Big Pine volcanic fields. The results are consistent with isotopic evidence from the literature for two distinct mantle sources, with the high-MgO potassic Kings River suite derived from Proterozoic North American CML, whereas the Long Valley and Big Pine basalts appear to have a source in CML that has been variably infiltrated with partial melts of asthenosphere.

Fourth, due to the absence of active subduction in the Pliocene, the source of the unusually high H₂O contents (~6-11 wt%) in the Kings River melts cannot be fluid released from a subducting slab. Nor could the high-water contents in these moderately potassic (mostly 2-4 wt% K₂O) basanites and minettes be derived solely from phlogopite in the mantle source region, since resulting partial melts would have ≤ 5 wt% H₂O and >6 wt% K₂O, which is insufficiently hydrous and too potassic to match the Kings River melt compositions. Instead, it may be that the location the Kings River volcanic field on top of the boundary between accreted Panthalassan oceanic lithosphere and Proterozoic North American continental lithosphere is relevant. Here it is proposed that lithosphere delamination beneath the southern Sierra Nevada in the Pliocene likely involved tectonic slices of serpentinized oceanic mantle, which released H₂O-rich fluid (due to dehydration of serpentine at $\leq 700^\circ\text{C}$ and 2-3 GPa) into the Proterozoic mantle source for the Kings River volcanic suite. An area of future work is to evaluate if this hypothesis can be tested using a geochemical signature imparted to the Kings River samples that can uniquely be tied to fluid released from serpentinized mantle versus phlogopite in metasomatized mantle (e.g., B, As, Sb; Scambelluri et al., 2019).

ACKNOWLEDGEMENTS

We thank Dr. Owen Neill for his expertise on electron microprobe analysis of mineral phases, which was central to this study. This work was supported by National Science Foundation grant EAR-2125941.

REFERENCES

- Allan, J.F., Batiza, R., Perfit, M.R., Fornari, D.J. & Sack, R.O. (1989). Petrology of lavas from the Lamont Seamount Chain and adjacent East Pacific Rise, 10°N. *Journal of Petrology*, 30, 1245–1298.
- Almeev, R.A., Holtz, F., Koepke, J., Parat, F. & Botcharnikov, R.E. (2007). The effect of H₂O on olivine crystallization in MORB: experimental calibration at 200 MPa. *American Mineralogist*, 92, 670-674.
- Asimow, P.D., Ghiorso, M.S., (1998). Algorithmic modifications extending MELTS to calculate subsolidus phase relations. *American Mineralogist*, 83, 9–10, 1127–1132.
- Atwater, T. & Stock, J. (1998). Pacific-North America Plate Tectonics of the Southwestern United States: An Update. *International Geology Review*, 40, 375-402
- Atwater, T. (1970). Implications of plate tectonics for the Cenozoic tectonic evolution of Western North America. *Geological Society of America Bulletin*, 81, 3513 – 3536.
- Beard, B. & Glazner A. (1995). Trace elements and Sr and Nd isotopic composition of mantle xenoliths from the Big Pine Volcanic Field, California. *Journal of Geophysical Research: Solid Earth*, 100, 4169-4179.

Beattie, P. (1993). Olivine-melt and orthopyroxene-melt equilibria. *Contributions to Mineralogy and Petrology*, 115, 103-111.

Berndt, J., Koepke, J. & Holtz, F. (2005). An experimental investigation of the influence of water and oxygen fugacity on differentiation of MORB at 200 MPa. *Journal of Petrology*, 46, 135–167.

Blundy, J., Melekhova, E., Ziberna, L., Humphreys, M.C.S., Cerantola, V., Brooker, R.A., McCammon, C.A., Pichavant, M. & Ulmer, P. (2020). Effect of redox on Fe-Mg-Mn exchange between olivine and melt and an oxybarometer for basalts. *Contributions to Mineralogy and Petrology*, 175, 103.

Brehm, S. & Lange, R.A. (2020). Rapid phenocryst growth in xenolith-bearing basalts from the Big Pine volcanic field, CA: application of olivine-melt oxybarometry, thermometry, and hygrometry at the liquidus. *Geochemistry, Geophysics, Geosystems*. 21.

Brehm, S. (2020). Evidence of rapid olivine phenocryst growth during ascent along fractures in Quaternary basalts from the basin and range extensional province: implications for the application of olivine-melt thermometry and hygrometry at the onset of phenocryst growth. University of Michigan, Doctoral Dissertation.

Condamine, P., Médard, E. & Devidal, J.-L. (2016). Experimental melting of phlogopite-peridotite in the garnet stability field. *Contributions to Mineralogy and Petrology*, 171, 1–26.

Condamine, P. & Médard, E. (2014). Experimental melting of phlogopite-bearing mantle at 1 GPa: Implications for potassic magmatism. *Earth and Planetary Science Letters*, 397, 80–92.

- Cousens B. (1996). Depleted and enriched upper mantle sources for basaltic rocks from diverse tectonic environments in the northeast Pacific Ocean: the generation of oceanic alkaline Vs. Tholeiitic basalts. *Geophys. Monogr. Ser.* 95, 207-231.
- Dickinson, W.R. & Lawton, T.F. (2001). Carboniferous to Cretaceous assembly and fragmentation of Mexico. *Geological Society of America Bulletin.* 113. 1142-1160.
- Ducea, M.N. & Saleeby, J.B. (1998a). The age and origin of a thick mafic-ultramafic keel from beneath the Sierra Nevada batholith. *Contributions to Mineralogy and Petrology*, 133, 169–185.
- Ducea, M.N. & Saleeby, J.B. (1998b). A case for delamination of the deep batholithic crust beneath the Sierra Nevada, California. *International Geology Review*, 40, 78-93.
- Ducea, M.N., & Saleeby, J.B. (1996). Buoyancy sources for a large, unrooted mountain range, the Sierra Nevada, California; evidence from xenolith thermobarometry. *Journal of Geophysical Research*, 101, 8229–8244.
- Elkins-Tanton, T. & Grove T. (2003). Evidence for deep melting of hydrous metasomatized mantle: Pliocene high-potassium magmas from the Sierra Nevadas. *Journal of Geophysical Research: Solid Earth*, 108, (9-1)-(9-19).
- Esperanca, S. & Holloway, J.R. (1987). On the origin of some mica-lamprophyres – experimental evidence from a mafic minette. *Contributions to Mineralogy and Petrology* 95(2), 201-216.
- Farmer, G. L., Glazner, A. F. & Manley, C. R. (2002). Did lithospheric delamination trigger late Cenozoic potassic volcanism in the southern Sierra Nevada, California? *Geological Society of American Bulletin*, v.114, no.6, 754-768.

- Faure, F., Trolliard, G., Nicollet, C. & Montel, J.-M. (2003). A developmental model of olivine morphology as a function of the cooling rate and the degree of undercooling. *Contributions to Mineralogy and Petrology*, 145, 251–263.
- Feldstein, S.N. & Lange, R.A. (1999). Pliocene potassic magmas from the Kings River region, Sierra Nevada, California: evidence for melting of a subduction-modified mantle. *Journal of Petrology*, 40, 1301–1320.
- Fleiderer M.M., Klemperer, S.L. & Christensen, N.I. (2000). Three-dimensional seismic model of the Sierra Nevada arc, California, and its implications for crustal and upper mantle composition. *Journal of Geophysical Research Solid Earth*, 105 (B5) 10,899-10,921.
- Frassetto, A.M., Zandt, G., Gilbert, H., Owens, T.J. & Jones, C.H. (2011). Lithospheric structure of the Sierra Nevada from receiver functions and implications for lithospheric foundering. *Geosphere*, 7, 898–921.
- Gavrilenko, M., Herzberg, C., Vidito, C., Carr, M.J., Tenner, T. & Ozerov, A. (2016). A calcium in-olivine geothermometer and its application to subduction-zone magmatism. *Journal of Petrology*, 57, 1811–1832.
- Gazel, E., Plank, T., Forsyth, D.W., Bendersky, C., Lee, C.T.A. & Hauri, E.H. (2012). Lithosphere versus asthenosphere mantle sources at the Big Pine Volcanic Field, California. *Geochemistry, Geophysics, Geosystems*, 13 (1), 1–25.
- Ghiorso, M.S. & Sack, R.O. (1995). Chemical mass transfer in magmatic processes IV. A revised and internally consistent thermodynamic model for the interpolation and extrapolation of liquid-solid equilibria in magmatic systems at elevated temperatures and pressures. *Contributions to Mineralogy and Petrology*, 119 (2–3), 197–212.

- Gilbert, H., Yang, Y., Forsyth, D.W., Jones, C., Owens, T., Zandt, G. & Stachnik, J. (2012). Imaging lithospheric foundering in the structure of the Sierra Nevada. *Geosphere*, 10.1130/GES00790.1.
- Haggerty, S. E. (1995). Upper mantle mineralogy. *Journal of Geodynamics*, Vol. 20, Issue 4, 331-364.
- Herzberg, C. & O'Hara, M.J. (2002). Plume-associated ultramafic magmas of Phanerozoic age. *Journal of Petrology*, 43, 1857–1883.
- Johnson, E.R., Wallace, P.J., Granados, H.D., Manea, V.C., Kent, A.J.R., Bindeman, I.N. & Donegan, C.S. (2009). Subduction-related volatile recycling and magma generation beneath Central Mexico: Insights from melt inclusions, oxygen isotopes and geodynamic models. *Journal of Petrology*, 50, 1729-1764.
- Jolles, J.S.R. & Lange, R.A. (2021). Temperatures and water contents of Long Valley, CA basalts: application of olivine-melt thermometry and hygrometry at the liquidus. *Journal of Volcanology and Geothermal Researcher*, 417, 107298.
- Kistler, R. (1990). Two different lithosphere types in the Sierra Nevada, California. *Geological Society of America*, Chapter 15.
- Lofgren, G. (1974). An experimental study of plagioclase crystal morphology; isothermal crystallization. *American Journal of Sciences*, 272, 243–273.
- Manley, C.R., Glazner, A.F. & Farmer, G.L., (2000). Timing of volcanism in the Sierra Nevada of California: evidence for Pliocene delamination of the basaltic root? *Geology* 28 (9), 811–814.

Maria, A.H. & Luhr, J.F. (2008). Lamprophyres, Basanites, and Basalts of the Western Mexican Volcanic Belt: Volatile Contents and a Vein–Wallrock Melting Relationship. *Journal of Petrology*, 49, 2123–2156.

McDonough, W. F. & Sun, S. S. (1995). The composition of the Earth. *Chemical Geology*, 120, 223–253.

Médard, E. & Grove, T.L. (2008). The effect of H₂O on the olivine liquidus of basaltic melts: experiments and thermodynamic models. *Contributions to Mineralogy and Petrology*, 155, 417–432.

Moore, G. & Carmichael, I.S.E. (1998). The hydrous phase equilibria (to 3 kbar) of an andesite and basaltic andesite from western Mexico: constraints on water content and conditions of phenocryst growth. *Contributions to Mineralogy and Petrology*, 130:304–319.

Moore, G. & Dodge F.C.W. (1981). Late Cenozoic volcanic rocks of the southern Sierra Nevada, California: 2. Geology and Petrology: summary. *Geological Society of America Bulletin*, 92, 912–914

Moore, G. & Dodge F.C.W. (1980). Late Cenozoic volcanic rocks of the southern Sierra Nevada, California: 1. Geology and Petrology: summary. *Geological Society of America Bulletin*, 91, 515–518.

Muñoz, M., Bureau, H., Malavergne, V., Menez, B., Wilke, M., Schmidt, C., Simionovici, A., Somogyi, A. & Farges, F. (2005). In-situ speciation of nickel in hydrous melts exposed to extreme conditions. *Physica Scripta*, 115, 921–922.

Neave, D.A. & Putirka, K.D. (2017). A new clinopyroxene-liquid barometer, and implications for magma storage pressures under Icelandic rift zones. *American Mineralogist* 102, 777–794.

- Ormerod, D.S., Rogers, N.W. & Hawkesworth, C.J. (1991). Melting in the lithospheric mantle: Inverse modelling of alkali-olivine basalts from the Big Pine volcanic field, California. *Contributions to Mineralogy and Petrology*, 108, 305-317.
- Parman, S.W., Grove, T.L., Kelley, K.A. & Plank, T. (2011). Along-arc variations in the pre-eruptive H₂O contents of Mariana Arc magma inferred from fractionation paths. *Journal of Petrology*, 52, 257-278.
- Pu, X., Lange, R.A. & Moore, G. (2017). A comparison of olivine-melt thermometers based on D_{Mg} and D_{Ni} : The effects of melt composition, temperature, and pressure with applications to MORBs and hydrous arc basalts. *American Mineralogist*, 102, 750–765.
- Pu, X., Moore, G.M., Lange, R.A., Touran, J.P. & Gagnon J.E. (2021). Experimental evaluation of a new H₂O-independent thermometer based on olivine-melt Ni partitioning at crustal pressure. *American Mineralogist*, 106 (2): 235–250.
- Pu, X., Lange, R.A., & Moore, G.M. (2023). Application of an improved olivine-melt thermometer/hygrometer to the Colima cone basanites and minettes of western Mexico: implications for the mantle source of unusually high-MgO melts. *Journal of Petrology* (in press).
- Putirka, K.D., Perfit, M., Ryerson, F.J. & Jackson, M.G. (2007). Ambient and excess mantle temperatures, olivine thermometry, and active vs. passive upwelling. *Chemical Geology*, 241, 177-206.
- Putirka, K.D. (2008) Thermometers and barometers for volcanic systems. In K.D. Putirka and F.J. Tepley III, Eds., *Minerals, Inclusions and Volcanic Processes*, 69, p. 61-120. *Reviews in Mineralogy and Geochemistry*, Mineralogical Society of America, Chantilly, Virginia.

Putirka, K.D. (2016). Rates and styles of planetary cooling on Earth, Moon, Mars, and Vesta, using new models for oxygen fugacity, ferric-ferrous ratios, olivine-liquid Fe-Mg exchange, and mantle potential temperature. *American Mineralogy*, 101, 819–840.

Putirka, K.D., Jean, M., Cousens, B., Sharma, R., Torrez, G., and Carlson, C. (2012) Cenozoic volcanism in the Sierra Nevada and Walker Lange, California, and a new model for lithospheric degradation. *Geosphere* 8 (2), 265-291.

Righter, K. & Carmichael, I.S.E. (1996). Phase equilibria of phlogopite lamprophyres from western Mexico: biotite-liquid equilibria and P-T estimates for biotite-bearing igneous rocks. *Contributions to Mineralogy and Petrology*, 123, 1-21.

Righter, K., Dyar, M. D., Delaney, J. S., Vennemann, T. W., Hervig, R. L. & King, P. L. (2002). Correlations of octahedral cations with OH⁺, O²⁺, Cl⁺, and F⁺ in biotite from volcanic rocks and xenoliths. *American Mineralogist* 87, 142-153.

Ruppert, S., Fliedner, M.M., & Zandt, G. (1998). Thin crust and active upper mantle beneath the southern Sierra Nevada in the western United States. *Tectonophysics*, 286, 237-252.

Saleeby, J. (1982). Polygenetic ophiolite belt of the California Sierra Nevada: Geochronological and tectonostratigraphic development. *Journal of Geophysical Research* 87, 1803-1824.

Scambelluri, M., Cannao, E., & Gilio, M. (2019). The water and fluid-mobile element cycles during serpentinite subduction. *European Journal of Mineralogy*, 31, 405-428.

Saleeby, J.B. (1992). Petrotectonic and paleogeographic settings of U.S. Cordilleran ophiolites, in Burchfiel, B.C, Lipman, P.W., and Zoback, M.L., eds., *The Cordilleran Orogen: Conterminous U.S.* Geological Society of America, *The Geology of North America*, G-3. 653-682.

- Saleeby, J. (2011). Geochemical mapping of the Kings-Kaweah ophiolite belt, California—Evidence for progressive mélangé formation in a large offset transform-subduction initiation environment. *Geological Society of America Special Paper 480*, 31-73.
- Shaw, H.F., Chen, J.H., Saleeby, J.B. & Wasserburg, G.J. (1987) Nd-Sr-Pb systematics and age of the Kings River ophiolite, California: implications for depleted mantle evolution. *Contributions to Mineralogy and Petrology* 96, 281-290.
- Shea, T., Hammer, J.E., Hellebrand, E., Mourey, A.J., Costa, F., First, E.C., Lynn, K.J. & Melnik, O. (2019). Phosphorous and aluminum zoning in olivine: contrasting behavior of two nominally incompatible trace elements. *Contributions to Mineralogy and Petrology*, 174 (85), 1–24.
- Sisson, T.W. & Grove, T.L. (1993a). Experimental investigations of the role of H₂O in calc-alkaline differentiation and subduction zone magmatism. *Contributions to Mineralogy and Petrology*, 113,143-166.
- Sisson, T.W. & Grove, T.L. (1993b). Temperatures and H₂O contents of low-MgO high-alumina basalts. *Contributions to Mineralogy and Petrology*, 113, 167-184.
- Sweeney, R.J., Thompson, A.B. & Ulmer, P. (1993). Phase relations of a natural MARID composition and implications for MARID genesis, lithospheric melting and mantle metasomatism. *Contr. Mineral. and Petrol.* 115, 225–241.
- Ulmer, P. & Trommsdorff, V. (1995). Serpentine stability to mantle depths and subduction related magmatism. *Science*, 268, 858-861.
- Van Kooten, G.K. (1980). Mineralogy, Petrology, and Geochemistry of an Ultrapotassic Basaltic Suite, Central Sierra Nevada, California, U.S.A. *Journal of Petrology*, 21, 651–684.

Van Kooten, G.K. (1981). Pb and Sr systematics of ultrapotassic and basaltic rocks from the central Sierra Nevada, California. *Contr. Mineral. And Petrol.* 76, 378-385.

Vigouroux, N., Wallace, P.J. & Kent, A.J.R. (2008). Volatiles in High-K Magmas from the Western Trans-Mexican Volcanic Belt: Evidence for Fluid Fluxing and Extreme Enrichment of the Mantle Wedge by Subduction Processes. *Journal of Petrology*, 49, 1589–1618.

Wagner, T.P., Donnelly-Nolan, J.M. & Grove, T.L. (1995). Evidence of hydrous differentiation and crystal accumulation in the low-MgO, high Al₂O₃ Lake Basalt from Medicine Lake volcano, California. *Contributions to Mineralogy and Petrology*, 121, 201-216.

Zandt, G., Gilbert, H., Owens, T., Ducea, M., Saleeby, J. & Jones, C. (2004). Active foundering of a continental arc root beneath the southern Sierra Nevada, California. *Nature*, 43, 41-45.

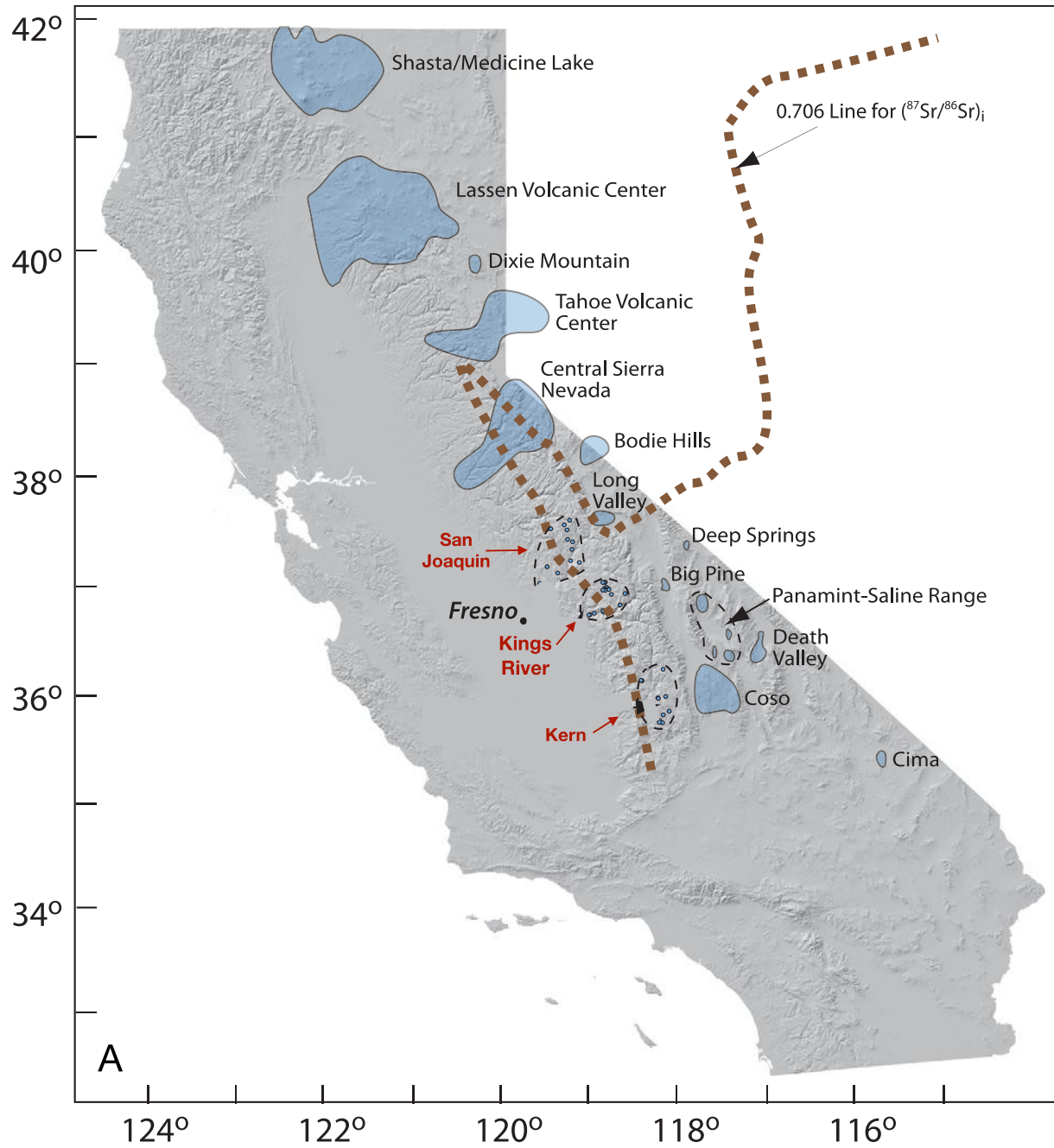


Figure 1A. Location map for the Kings River volcanic field, modified from Putirka et al. (2017). It is one of three southern Sierra volcanic fields; San Joaquin is to the north and Kern is to the south. Note their location along the boundary (denoted by 0.706 Sr isotopic line of Kistler, 1990) between the accreted, Panthalassan oceanic lithosphere to the west and North American continental lithosphere to the east.

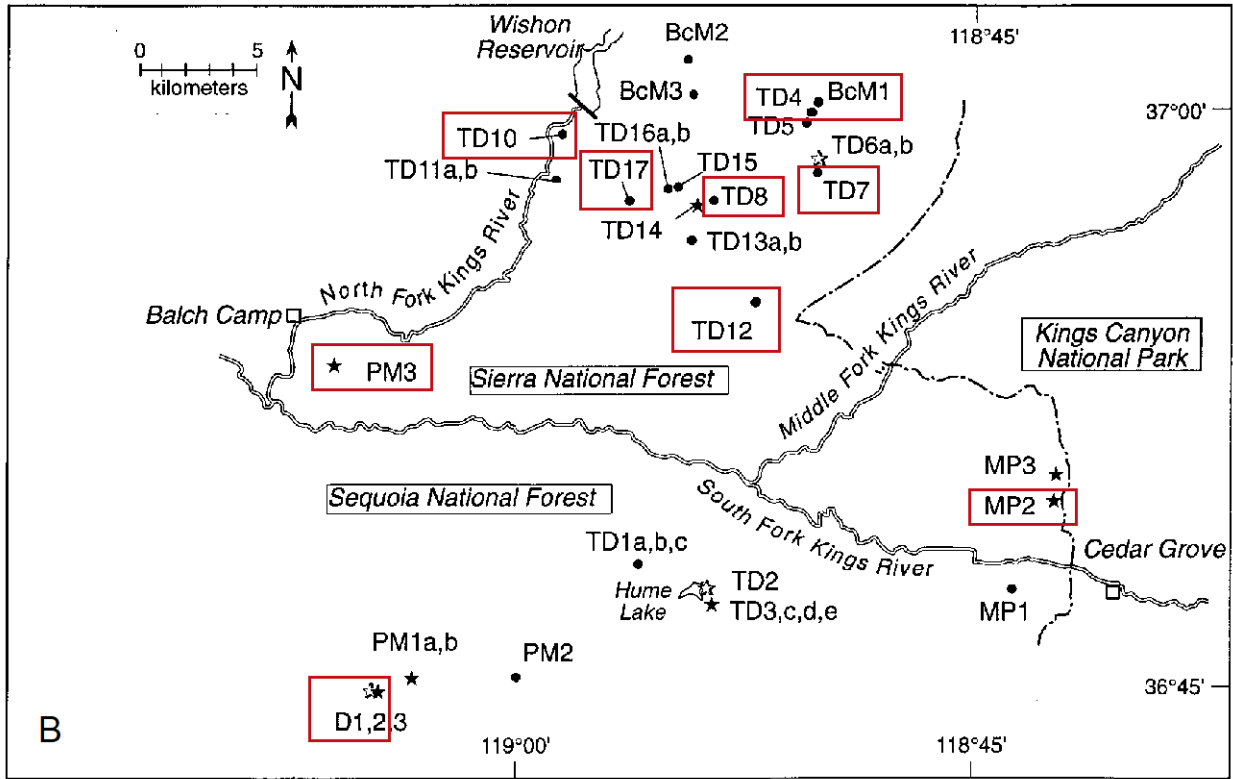


Figure 1B. Blow-up of the Pliocene Kings River volcanic field, showing the location of volcanic flows sampled by Feldstein and Lange (1999). Samples enclosed in red boxes are those used in this study.

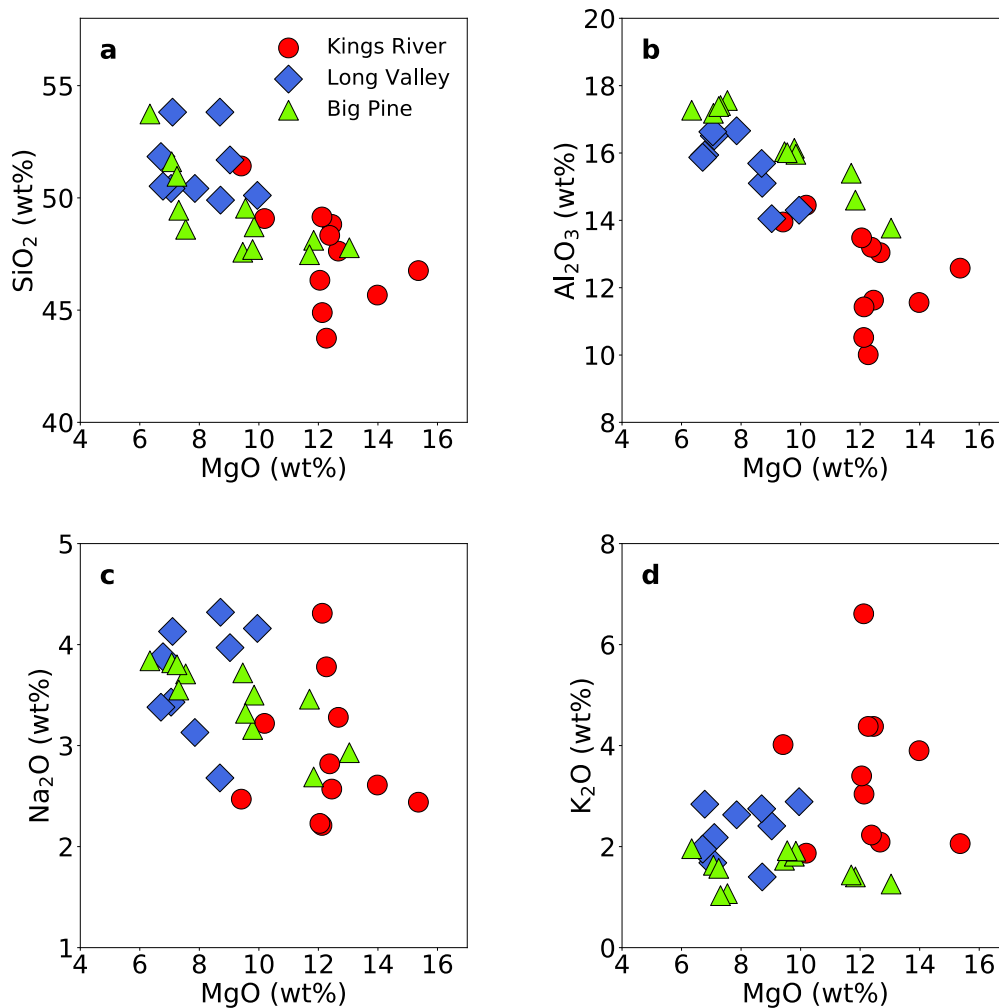


Figure 2. Figure 2 Whole-rock (a) SiO₂, (b) Al₂O₃, (c) Na₂O, (d) K₂O contents versus MgO content for Kings River shown in red circles. Whole rock contents versus MgO in Long Valley, Ca basalts (Jolles and Lange, 2021) are shown in blue diamonds. Whole rock contents versus MgO in Big Pine samples (Brehm and Lange, 2020) are shown in green diamonds. In comparison to the typical samples from Long Valley and Big Pine, the King River samples have higher MgO (up to 15.36 wt%) and K₂O (up to 6.6 wt%) and lower Al₂O₃ (down to 10.0 wt%) and SiO₂ (down to 43.8 wt%).

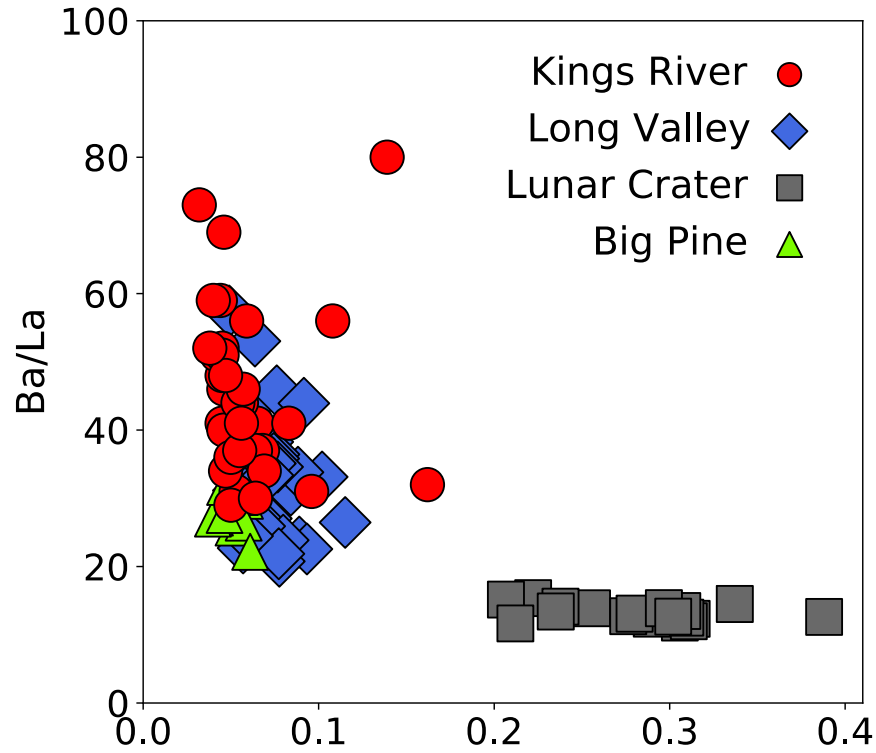


Figure 3. Whole-rock Ba/La ratio versus Nb/Zr ratio of samples from Kings River shown in red circles, Long Valley (Jolles and Lange, 2021) shown in blue diamonds, Big Pine (Brehm and Lange, 2020) shown in green diamonds, and Lunar Crater samples (Cortés et al., 2015) shown in gray squares. Lv, BP and KR basalts have an arc geochemical signature (enriched in slab-fluid component), consistent with subduction-modified lithosphere source, whereas Lunar Crater samples plot separately, consistent with an asthenosphere source.

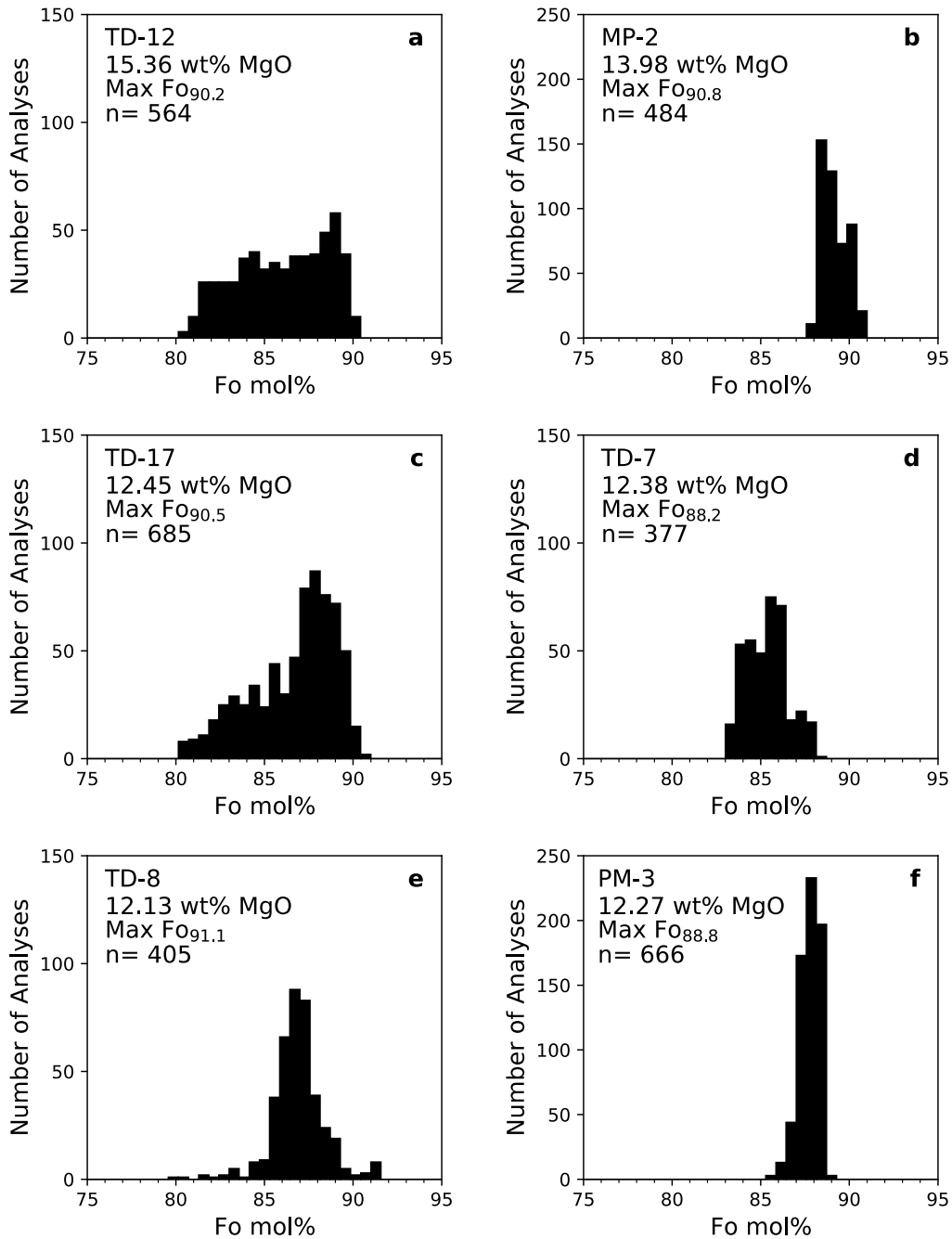


Figure 4A-F. Histograms of forsterite ($\text{Fo mol\%} = \frac{\text{XMgO}}{\text{XMgO} + \text{XFeO}} \times 100$) content of olivine crystals for six King River volcanic field samples. The most Fo-rich crystal in each sample was used for olivine melt thermometry (Pu et al., 2017). Because only the most Mg-rich olivine crystals were targeted for analysis, histograms only represent the Mg-rich part of olivine population.

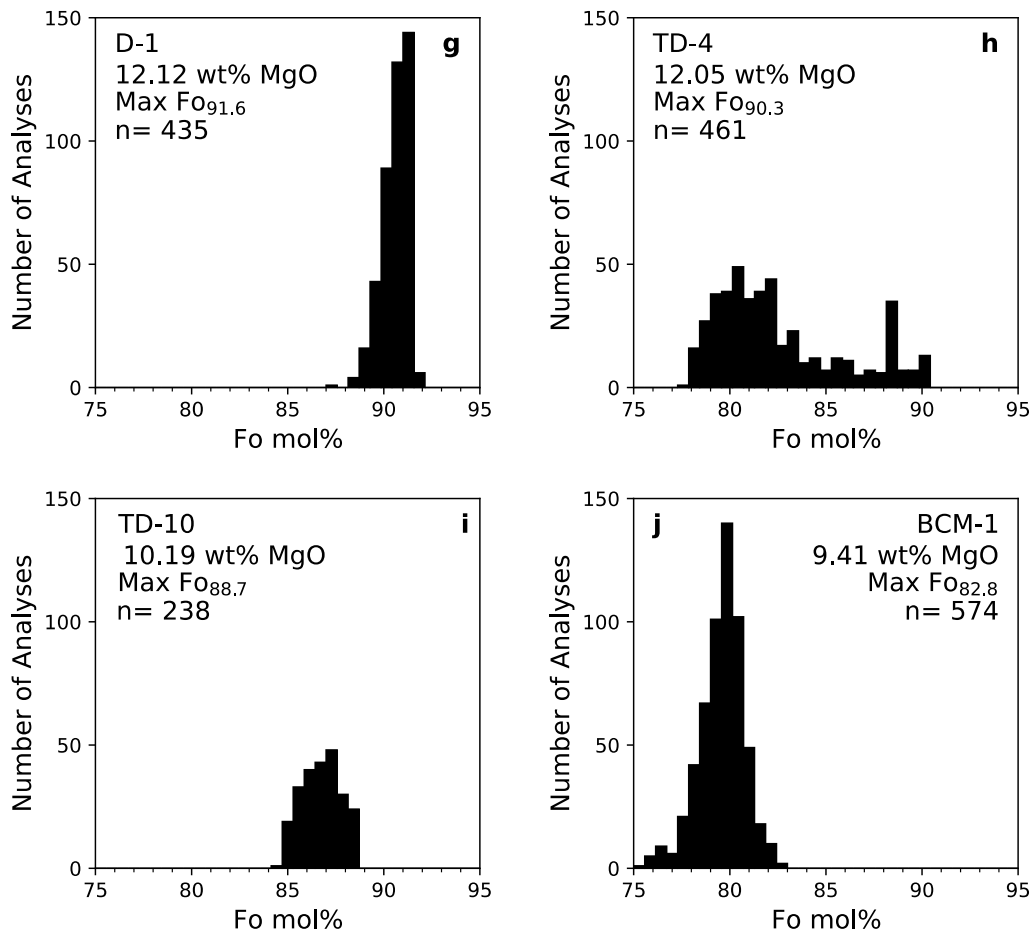


Figure 4G-I. Histograms of forsterite ($\text{Fo mol\%} = \frac{\text{XMgO}}{\text{XMgO} + \text{XFeO}} \times 100$) content of olivine crystals for four King River volcanic field samples. The most Fo-rich crystal in each sample was used for olivine melt thermometry (Pu et al., 2017). Because only the most Mg-rich olivine crystals were targeted for analysis, histograms only represent the Mg-rich part of olivine population.

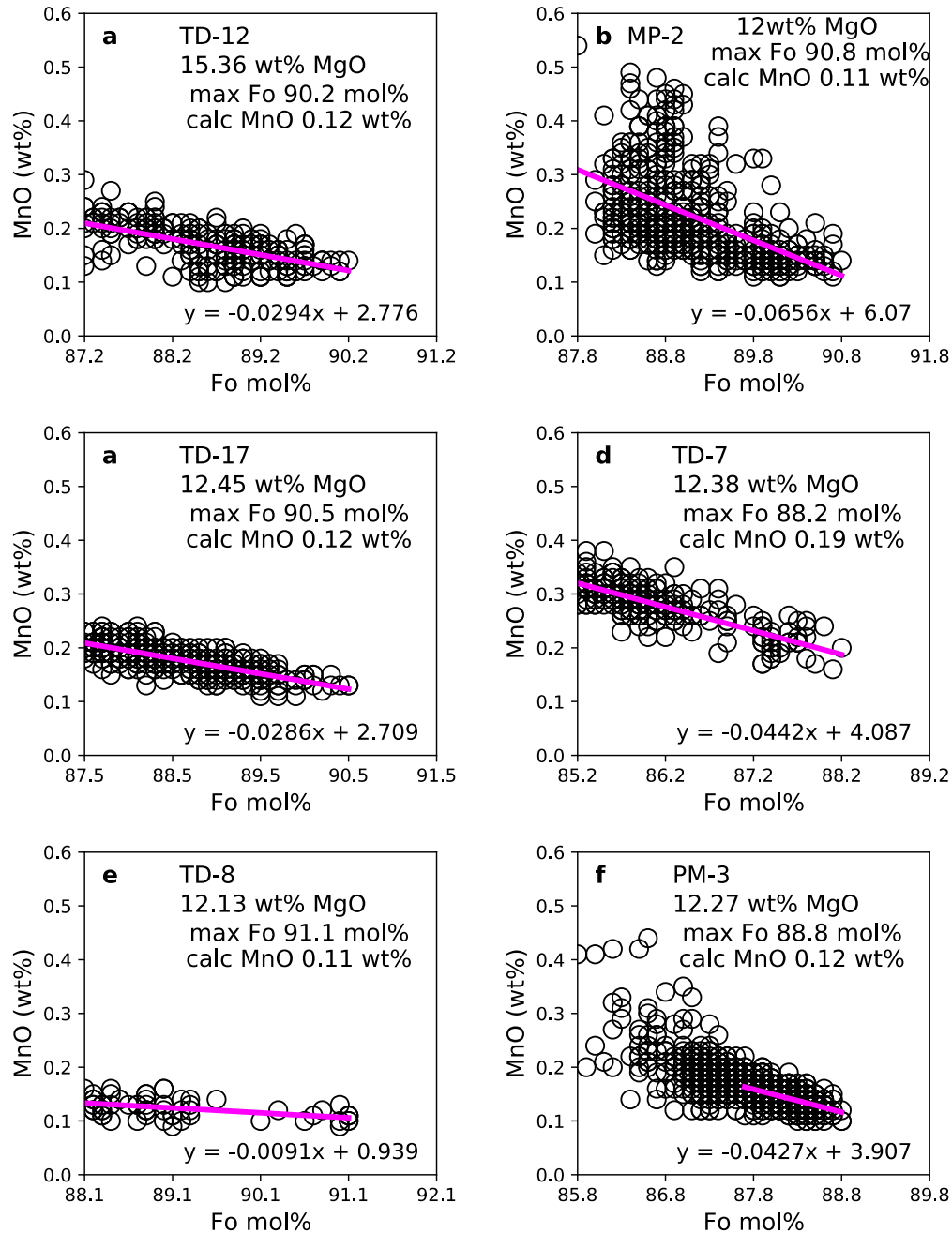


Figure 5A-F. Plots of MnO (wt%) vs Fo content in olivine for the highest 3 mol% Fo in each sample. A linear fit to the top 3 mol% of analyzed olivine in each sample (red line) is used to calculate the MnO wt% for the most Mg-rich olivine in each sample (Table 3). A linear fit of the top 1 mol% of analyzed olivine in Pm-3 (red line) is used to calculate the MnO wt% for the most Mg-rich olivine. This calculated MnO content is used to calculate the Mn-Mg exchange coefficient between olivine and melt at liquidus conditions (Table 3), in a test of equilibrium using the Blundy et al. (2020) model.

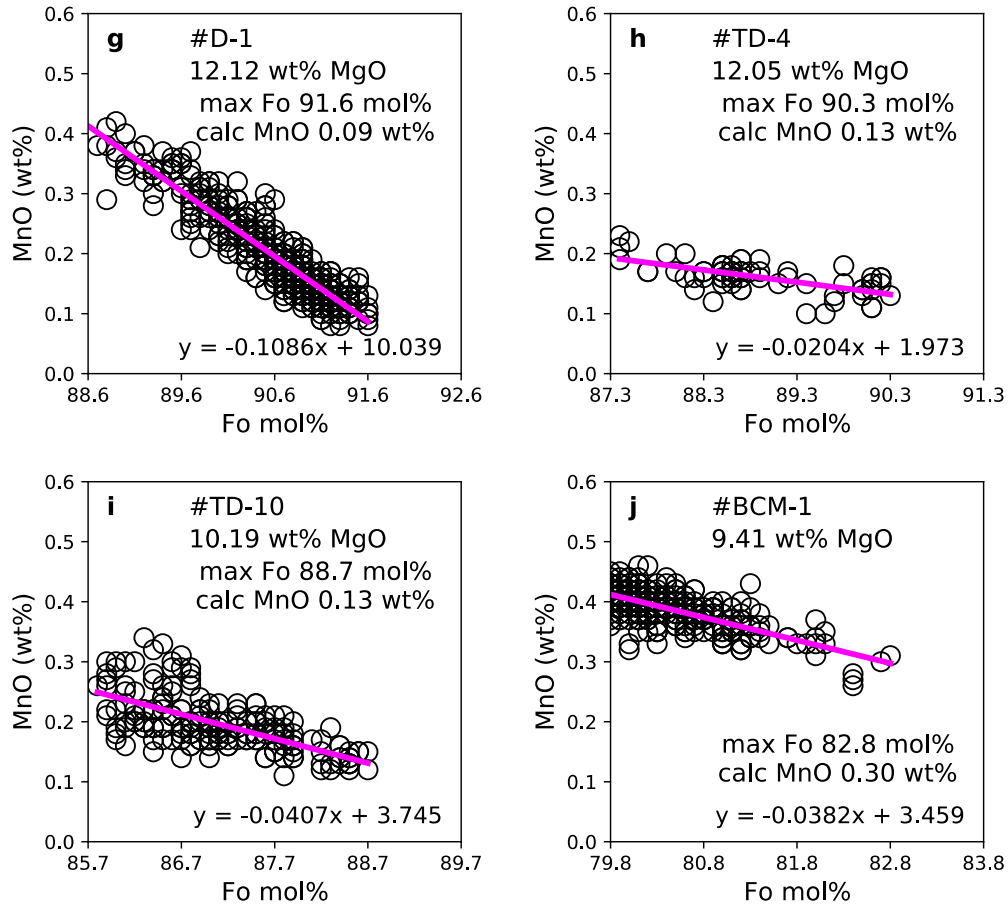


Figure 5G-J. Plots of MnO (wt%) vs Fo content in olivine for the highest 3 mol% Fo in each sample. A linear fit to the top 3 mol% of analyzed olivine in each sample (red line) is used to calculate the MnO wt% for the most Mg-rich olivine in each sample (Table 3). This calculated MnO content is used to calculate the Mn-Mg exchange coefficient between olivine and melt at liquidus conditions (Table 3), in a test of equilibrium using the Blundy et al. (2020) model.

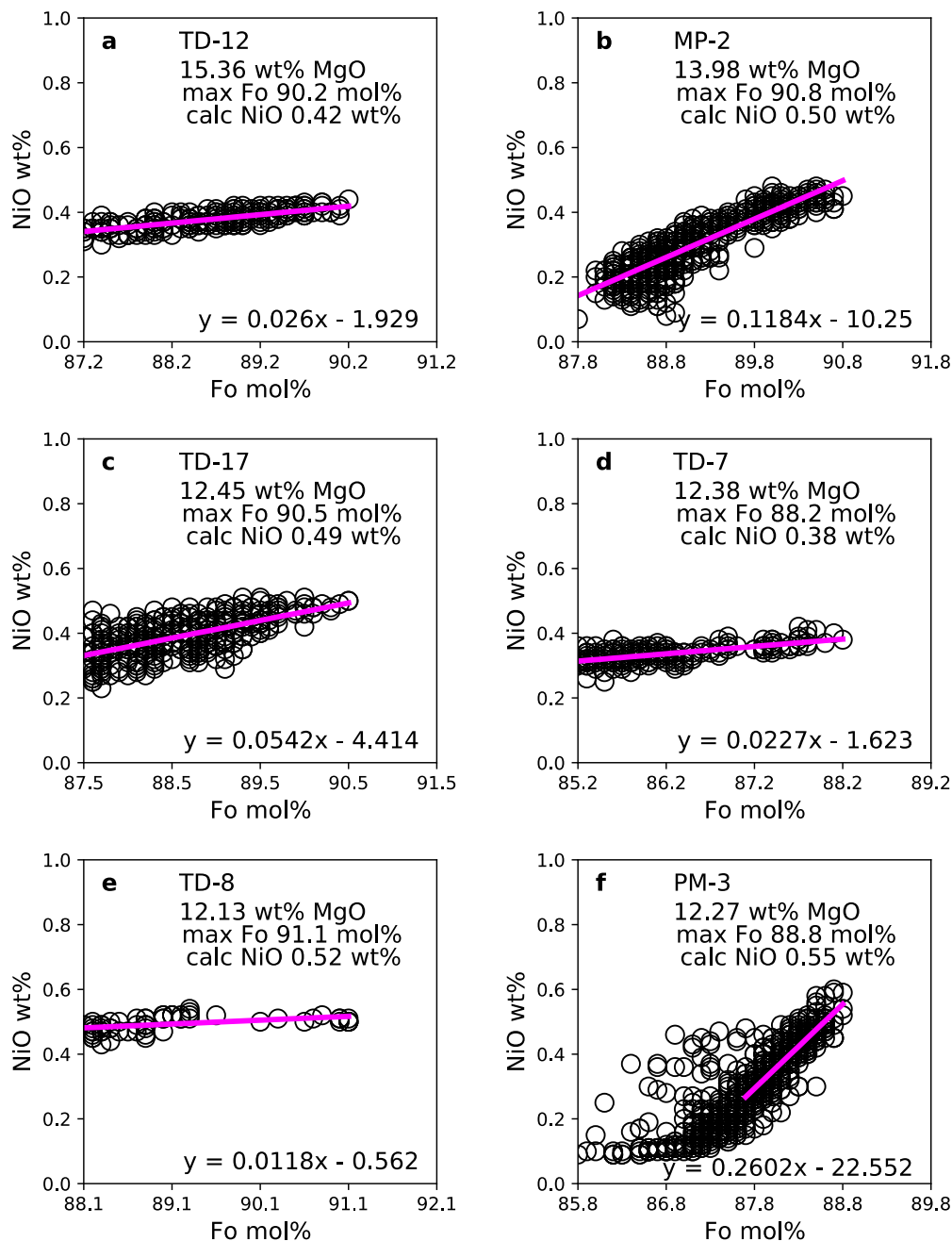


Figure 6A-F. Plots of NiO (wt%) vs Fo content in olivine for the highest 3 mol% Fo in each sample. A linear fit to the top 3 mol% of analyzed olivine in each sample (red line) is used to calculate the NiO wt% for the most Mg-rich olivine in each sample (Table 3). A linear fit of the top 1 mol% of analyzed olivine in PM-3 (red line) is used to calculate the NiO wt% for the most Mg-rich olivine. This calculated NiO content is used to calculate $DNi_{(ol-liq)}$ for the application of the olivine-melt Ni thermometer.

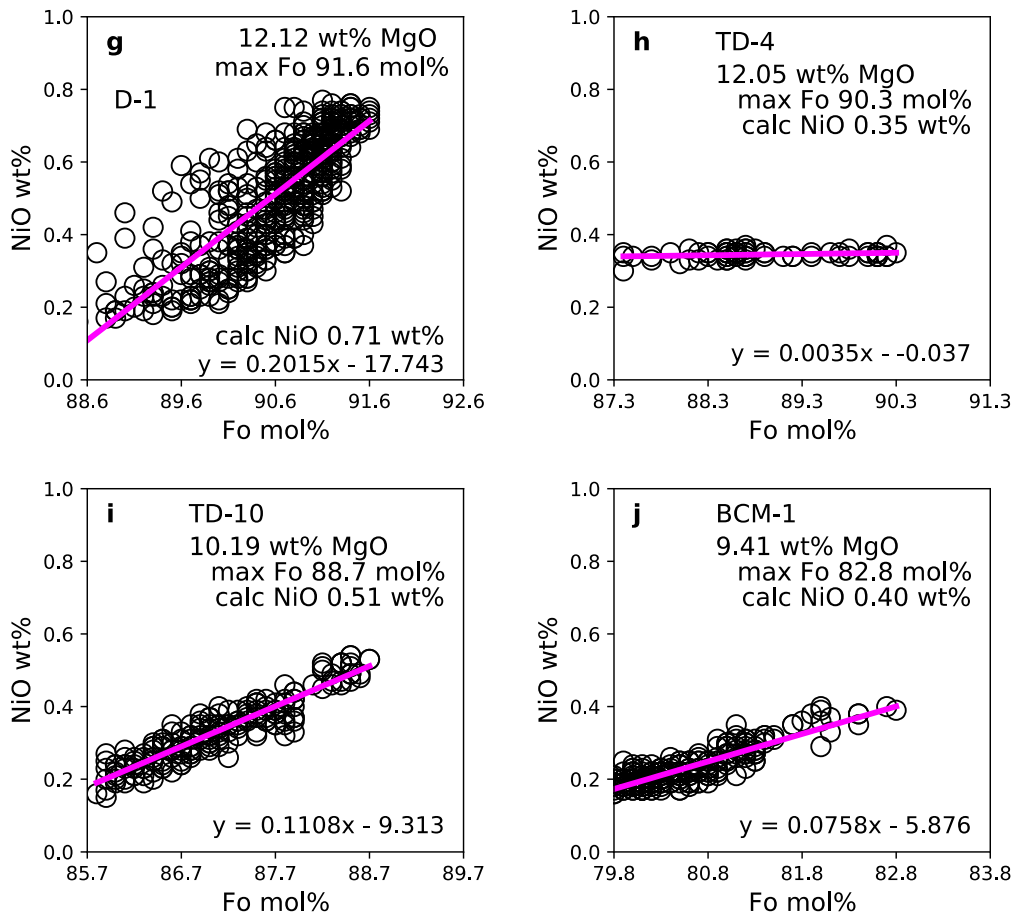


Figure 6.G-J Plots of NiO (wt%) vs Fo content in olivine for the highest 3 mol% Fo in each sample. A linear fit to the top 3 mol% of analyzed olivine in each sample (red line) is used to calculate the NiO wt% for the most Mg-rich olivine in each sample (Table 3). This calculated NiO content is used to calculate DN_i (ol-liq) for the application of the olivine-melt Ni thermometer.

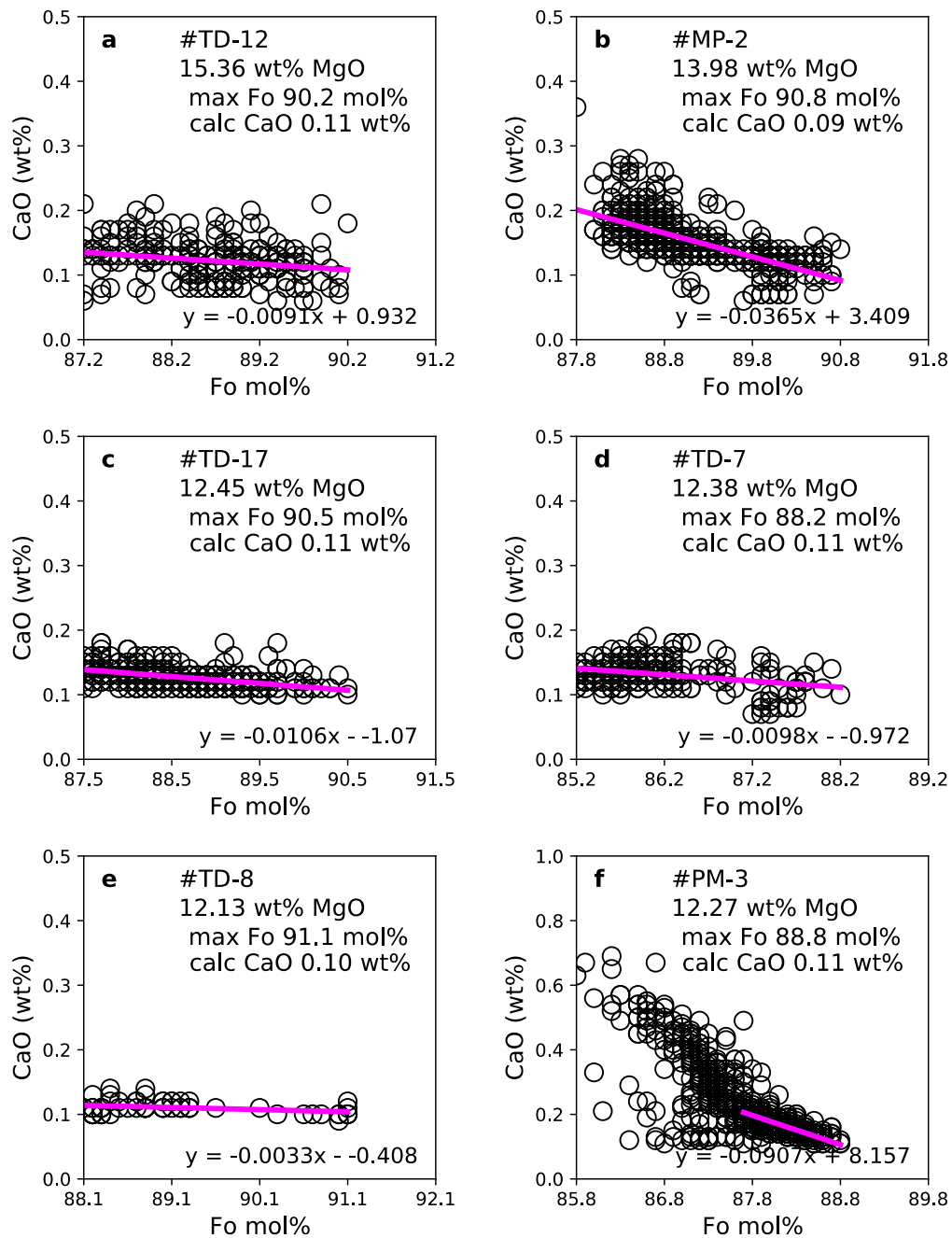


Figure 7A-F. Plots of CaO (wt%) vs Fo content in olivine for the highest 3 mol% Fo in each sample. A linear fit to the top 3 mol% of Fo of analyzed olivine in each sample (red line) is used to calculate the CaO wt% for the most Mg-rich olivine in each sample. A linear fit of the top 1 mol% of analyzed olivine in PM-3 (red line) is used to calculate the NiO wt% for the most Mg-rich olivine (Table 3).

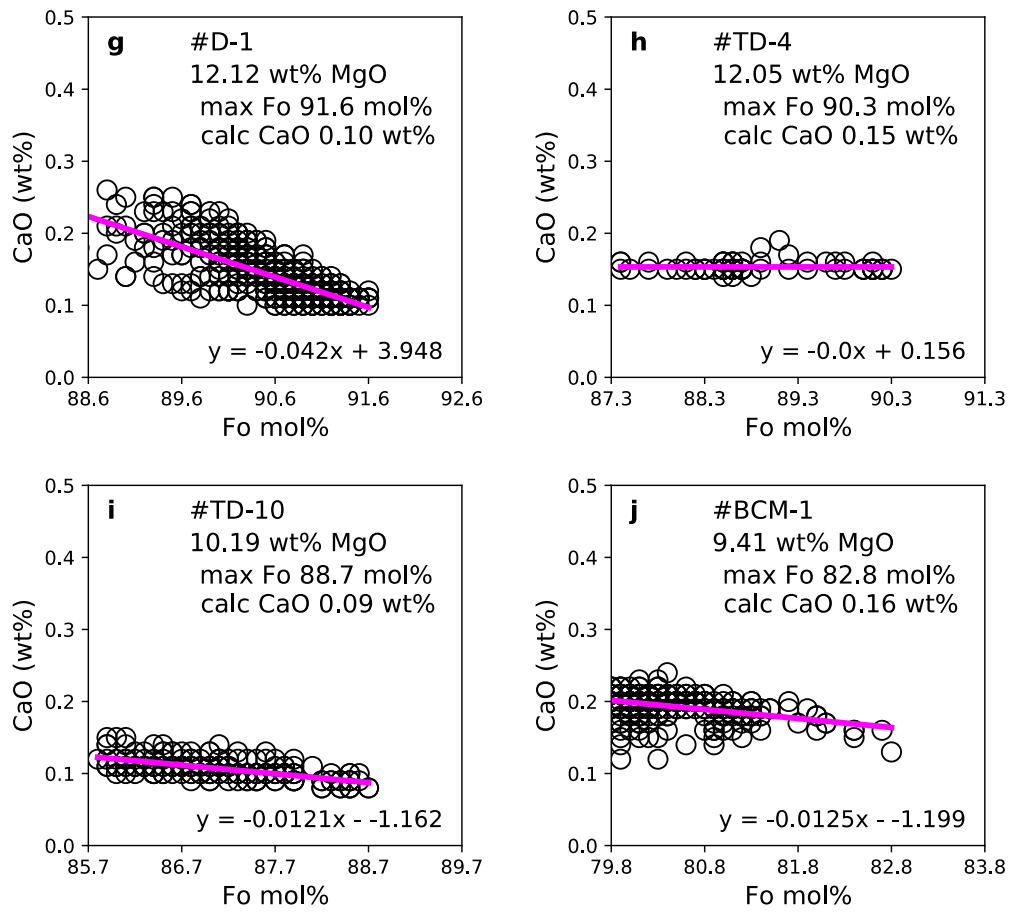


Figure 7G-J. Plots of CaO (wt%) vs Fo content in olivine for the highest 3 mol% Fo in each sample. A linear fit to the top 3 mol% of Fo of analyzed olivine in each sample (red line) is used to calculate the CaO wt% for the most Mg-rich olivine in each sample (Table 3).

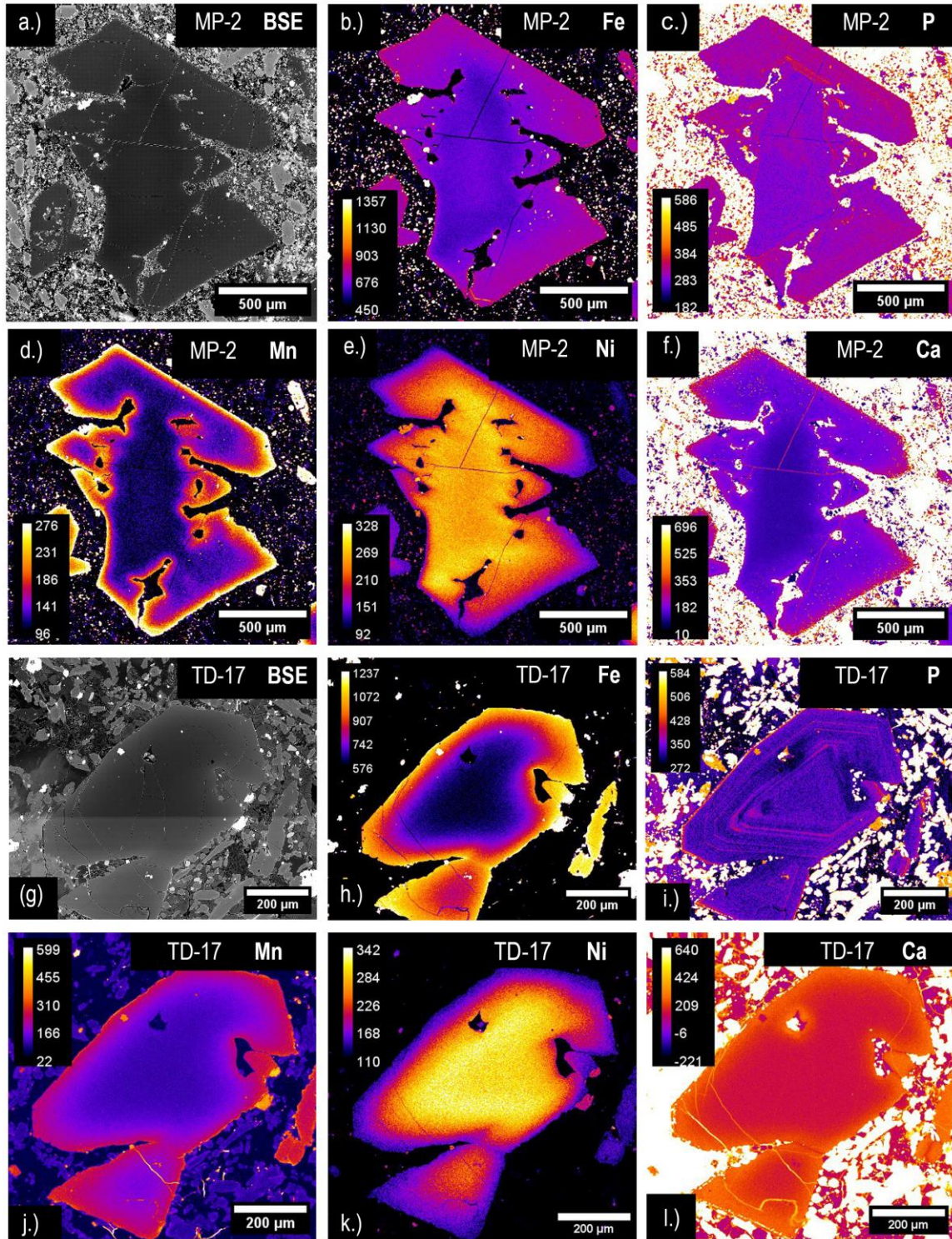


Figure 8A-L. Samples MP-2 Oliv 28 (a-f) and TD-17 Oliv 68 (g-l). Back scattered electron (BSE) images (a, g), X-ray intensity map of Fe (b,h) P (c, i), Mn (d, j), Ni (e, k) and Ca (f, l) in Mg rich olivine from two Kings River samples.

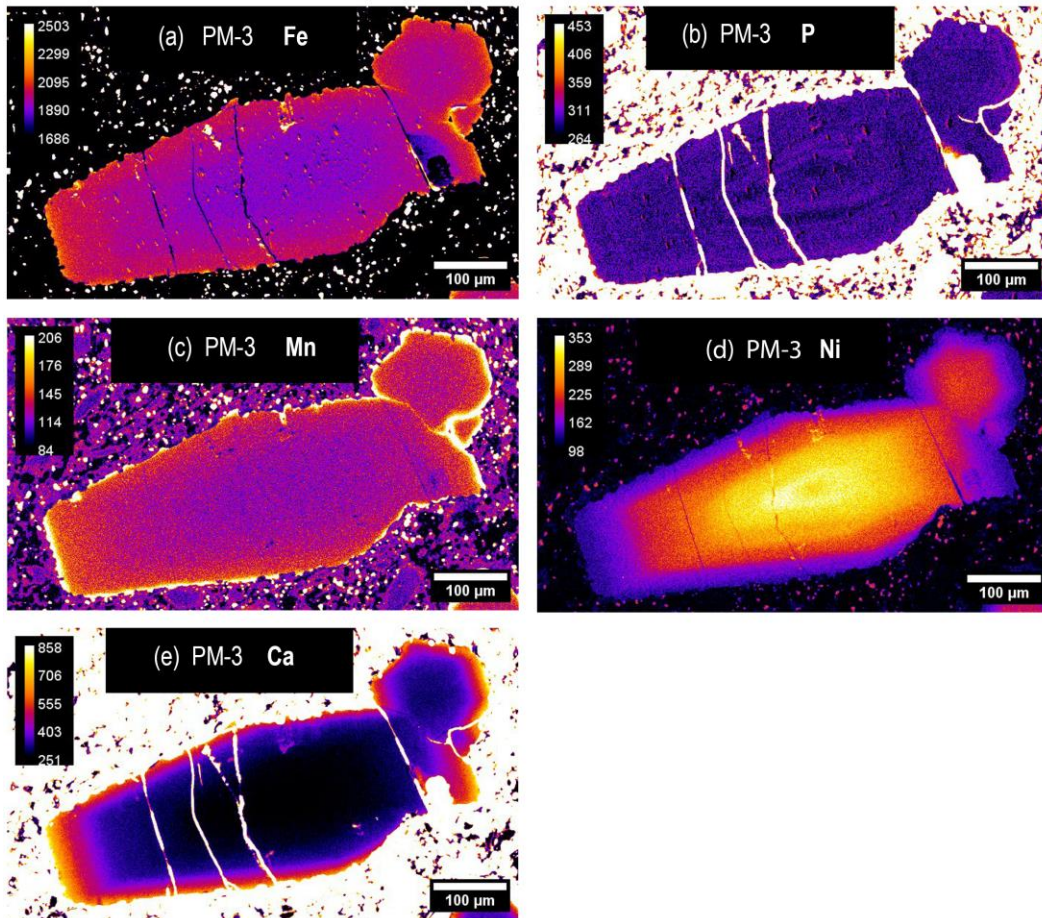


Figure 9A-E. Sample PM-3 Olv-21 X-ray intensity maps of Fe (a) P (b), Mn (c), Ni (d) and Ca (e) in an Mg rich olivine crystal.

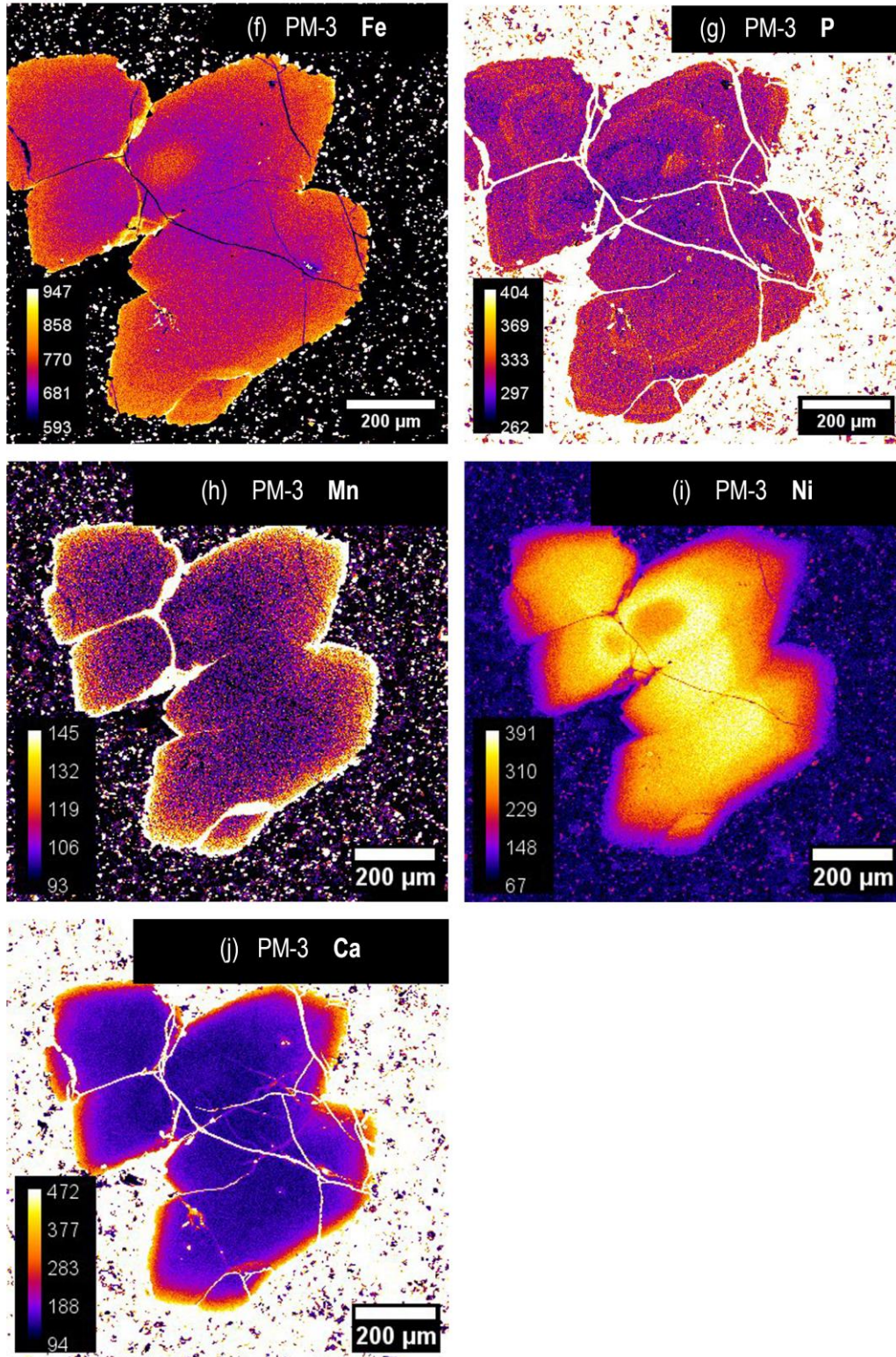


Figure 9F-J. Sample PM-3 Olv-69 X-ray intensity maps of Fe (f) P (g), Mn (ch, Ni (i) and Ca (j) in an Mg rich olivine crystal.

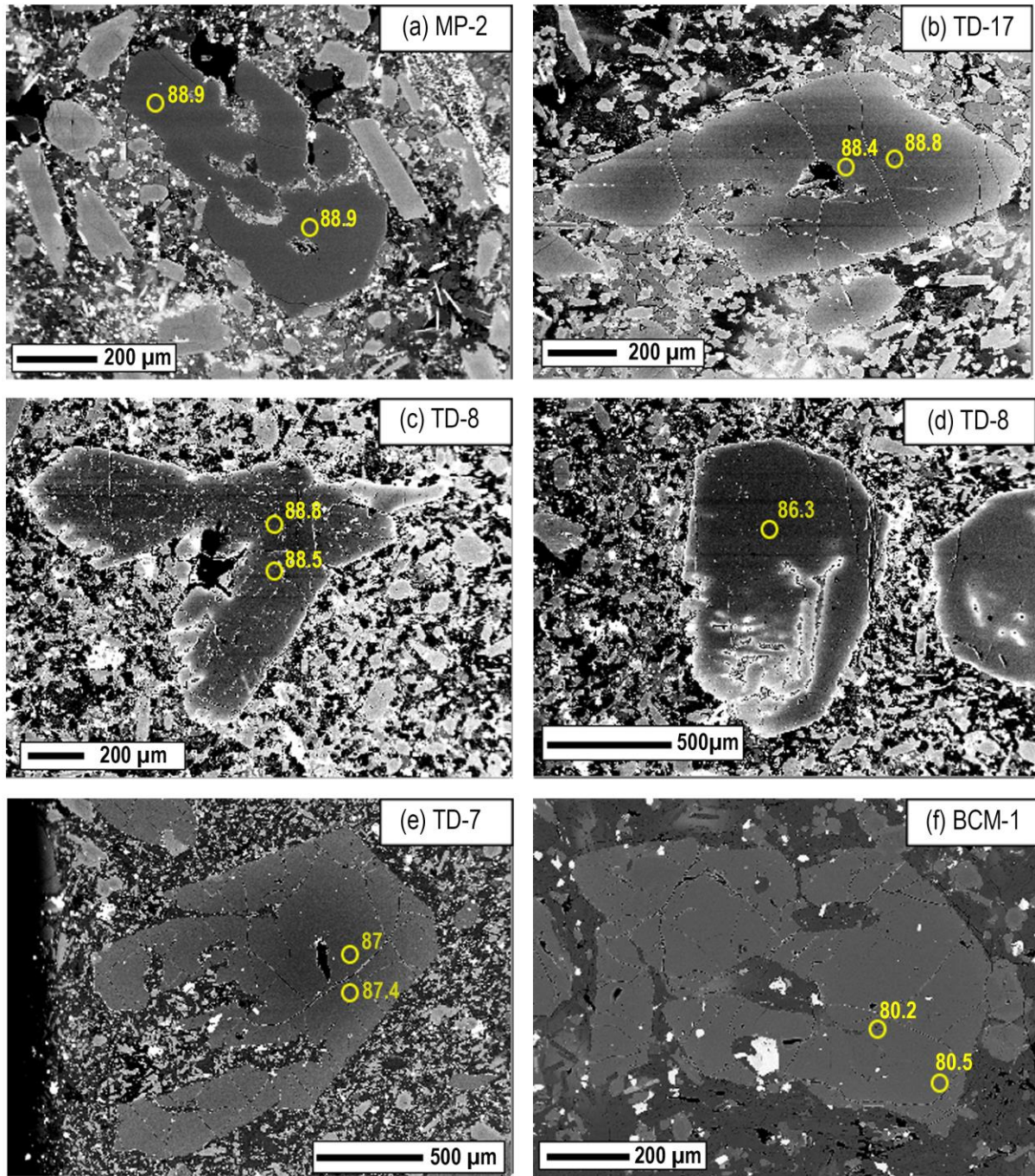


Figure 10A-F. Back scattered electron (BSE) image of representative olivine phenocrysts from six King River samples. Representative spot analyses are shown. The crystals in (a), (b), (c) (d) (e), (f) show rapid-growth hopper and skeletal textures.

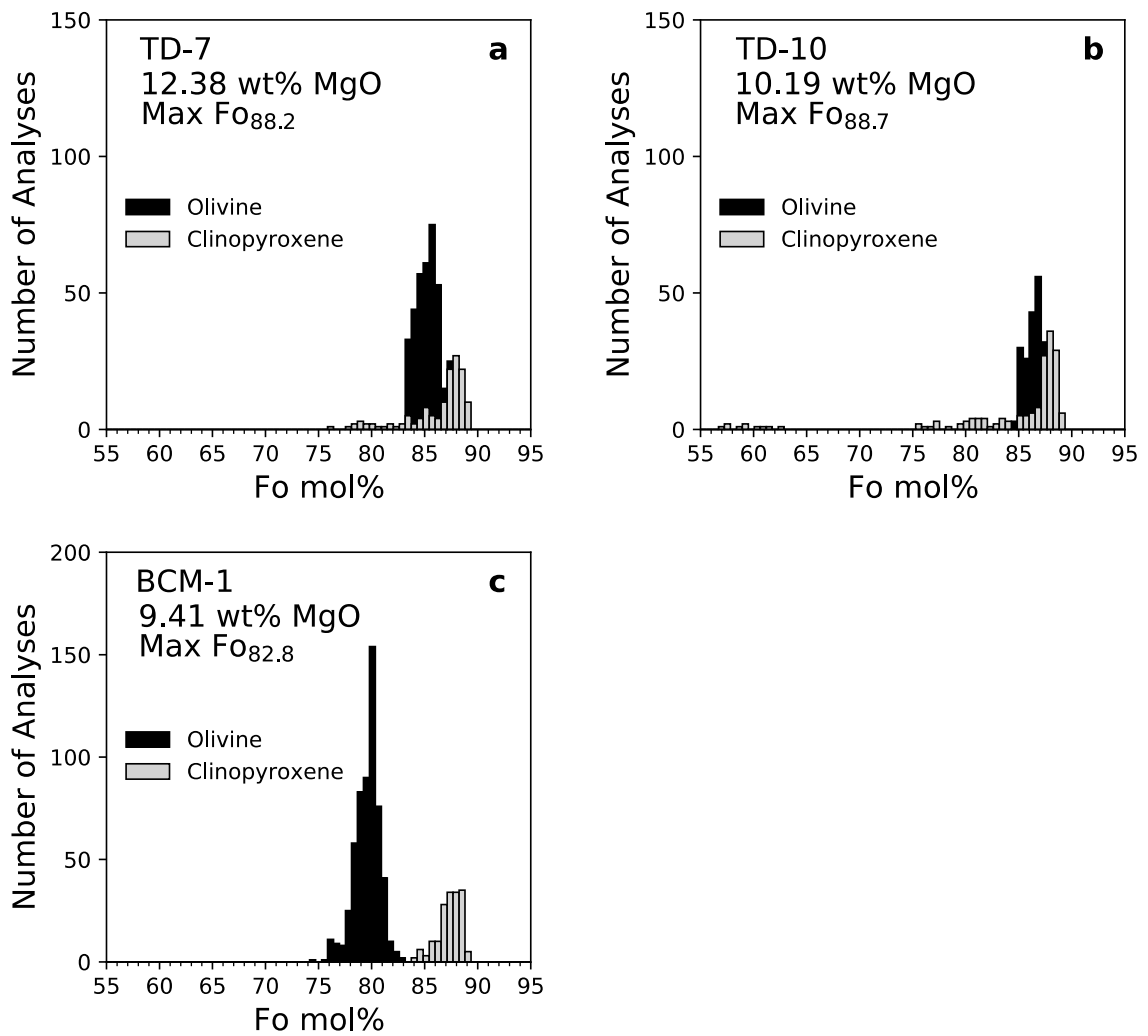


Figure 11A-C. Histograms of forsterite content ($\text{Fo mol\%} = \frac{X_{\text{MgO}}}{X_{\text{MgO}} + X_{\text{FeO}}} \cdot 100$) of olivine crystals (black) and Mg # of clinopyroxene crystals (red) for three samples from the King River volcanic field.

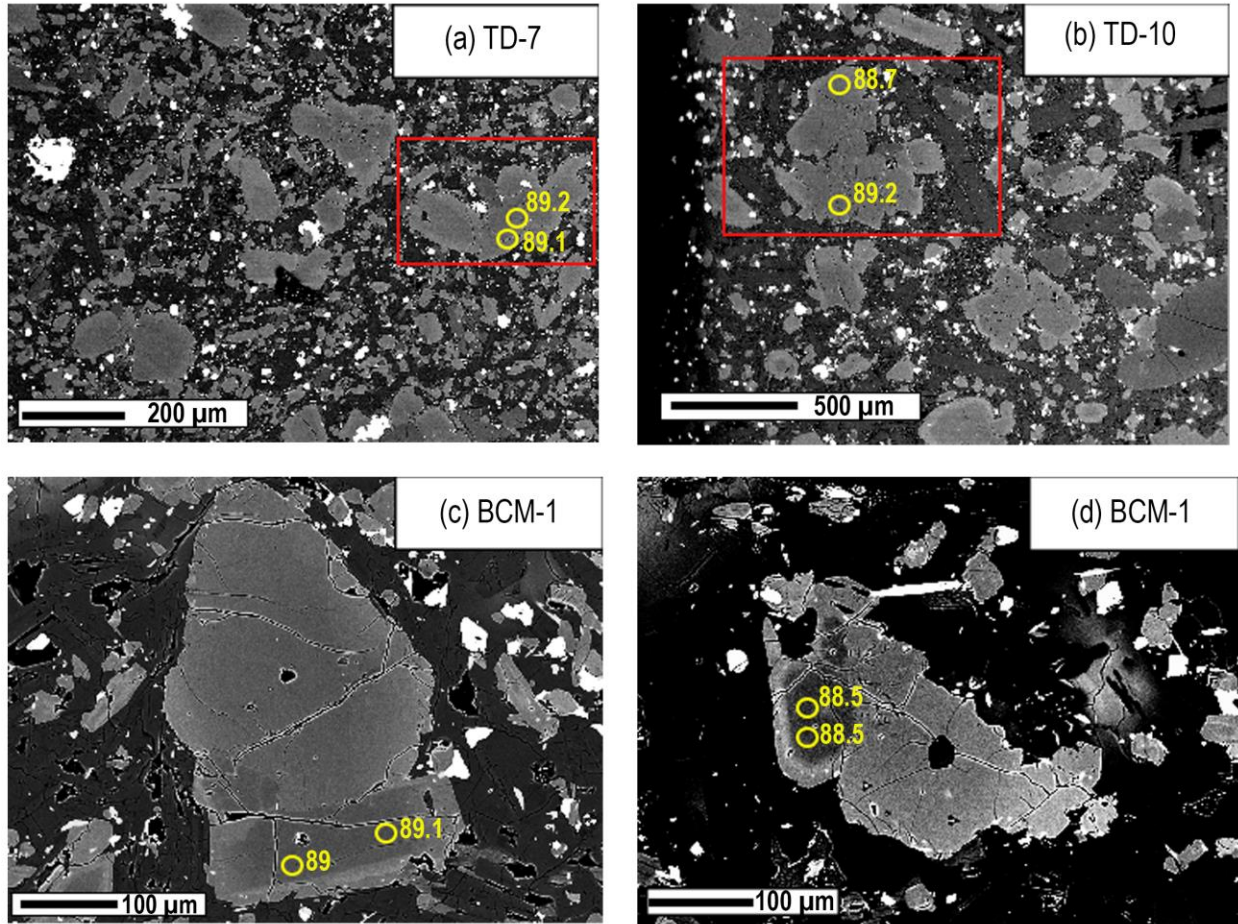


Figure 12A-D. Representative backscattered electron (BSE) images of most Mg-rich clinopyroxene crystals from samples TD-7, TD-17 and BCM-1. (a–b) Crystals with dark cores. (c–d) BCM-1 samples show clinopyroxene encased in olivine.

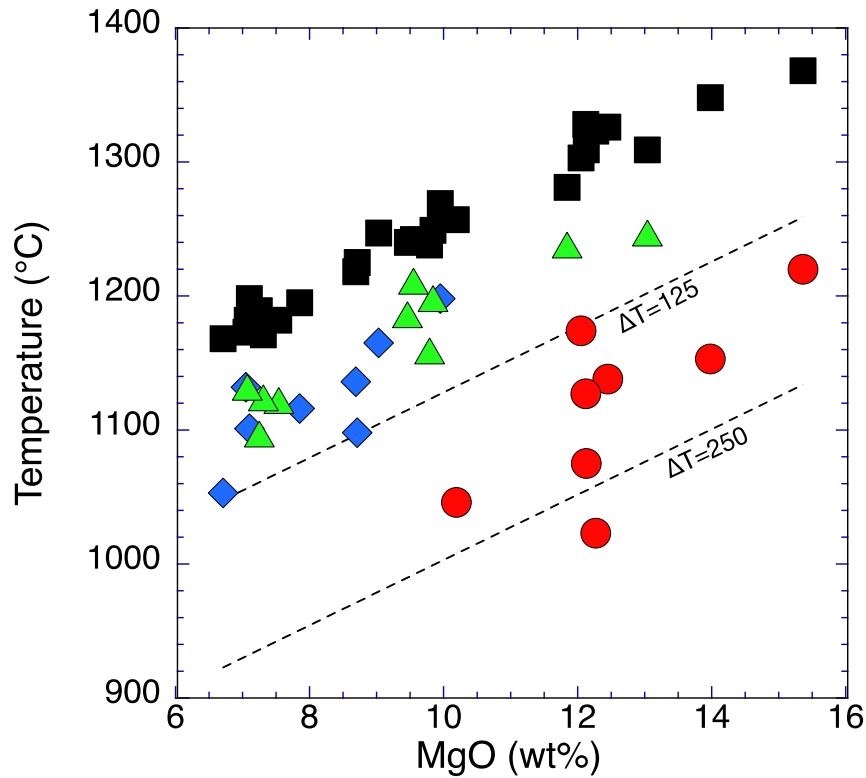


Figure 13. Calculated temperatures ($^{\circ}\text{C}$) at the onset of olivine crystallization (i.e., liquidus) from the olivine-melt Mg- and Ni-thermometers (Pu et al., 2017) versus whole-rock MgO (wt%) content. All T_{Mg} temperatures are shown in black squares. T_{Ni} temperatures for the Kings River samples from this study are shown in red circles. T_{Ni} temperatures for the Long Valley, CA basalts (Jolles and Lange, 2021) are shown in blue diamonds. T_{Ni} temperatures for the Big Pine samples (Brehm and Lange, 2020) are shown in green triangles. Because T_{Mg} is the temperature under anhydrous conditions and T_{Ni} is the actual temperature, the difference between them ($\Delta T = T_{Mg} - T_{Ni}$) reflects the depression of the olivine liquidus with dissolved H_2O content. Note that most of the Kings River samples have ΔT values that exceed 125°C , whereas most Long Valley and Big Pine basalts have ΔT values below 125°C .

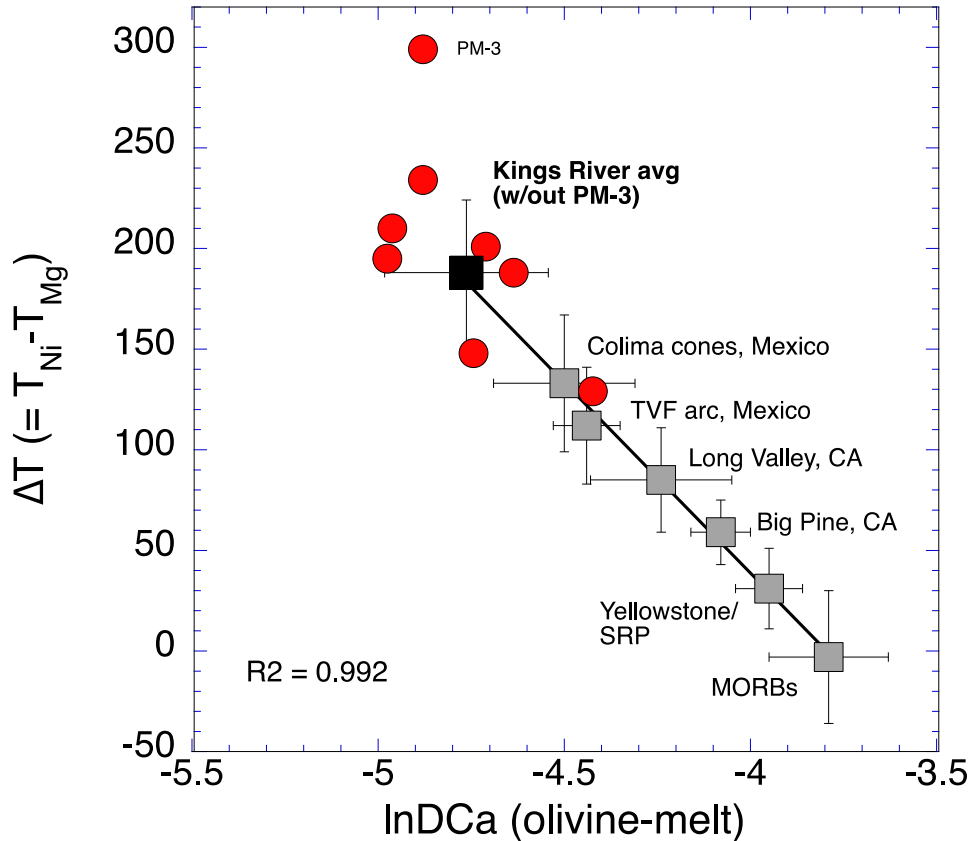


Figure 14A. (a) Average $\Delta T (=T_{Mg} - T_{Ni})$ versus average $\ln D_{Ca}^{oliv/liq}$ for several volcanic fields. Kings River volcanic field (black square; this study); Colima cone volcanic field in Mexican arc (Pu et al., 2023); Tancitaro volcanic field in Mexican arc (TVF; Pu et al., 2017); Long Valley, CA (Jolles & Lange, 2021); Big Pine, CA (Brehm and Lange, 2020); Yellowstone and Eastern Snake River Plain (Y/ESRP; Brehm, 2021); central Atlantic mid-ocean ridge basalts (MORB; Allan et al., 1989; Pu et al., 2017). Larger ΔT (reflecting depression of the olivine liquidus) correlates to lower $D_{Ca}^{oliv/liq}$. Linear fit to the average of all seven volcanic fields has $R^2 = 0.992$. Individual Kings River samples are shown in red. Note that PM-3 may be an outlier since its Ni content was not measured by the more accurate XRF method.

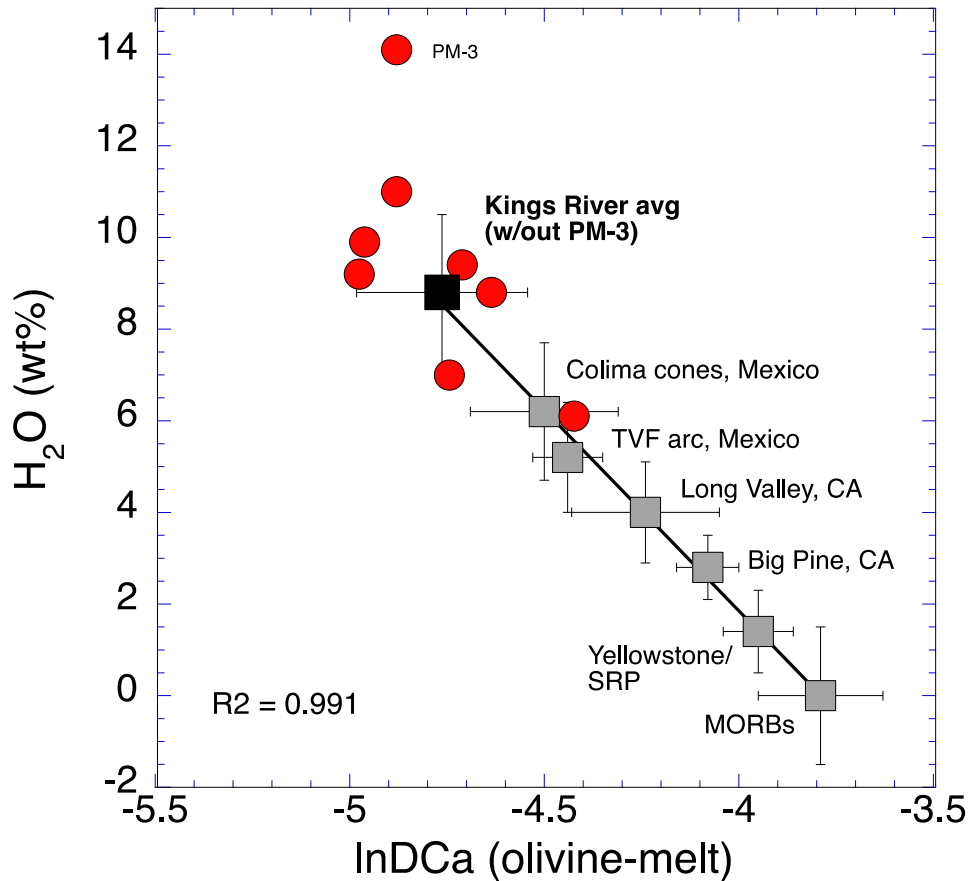


Figure 14B. (a) Average H₂O wt% (calculated from ΔT values in Fig. 14A) versus average $\ln D_{Ca}^{oliv/liq}$ for several volcanic fields. Kings River volcanic field (black square; this study); Colima cone volcanic field in Mexican arc (Pu et al., 2023); Tancitaro volcanic field in Mexican arc (TVF; Pu et al., 2017); Long Valley, CA (Jolles & Lange, 2021); Big Pine, CA (Brehm and Lange, 2020); Yellowstone and Eastern Snake River Plain (Y/ESRP; Brehm, 2021); central Atlantic mid-ocean ridge basalts (MORB; Allan et al., 1989; Pu et al., 2017). Larger H₂O contents in the melt correlates to lower $D_{Ca}^{oliv/liq}$, as previously noted by Gavrilenko et al. (2016). Linear fit to the average of all seven volcanic fields has $R^2 = 0.991$. Individual Kings River samples with olivine on liquidus are shown in red. Note that PM-3 may be an outlier since its Ni content was not measured by the more accurate XRF method.

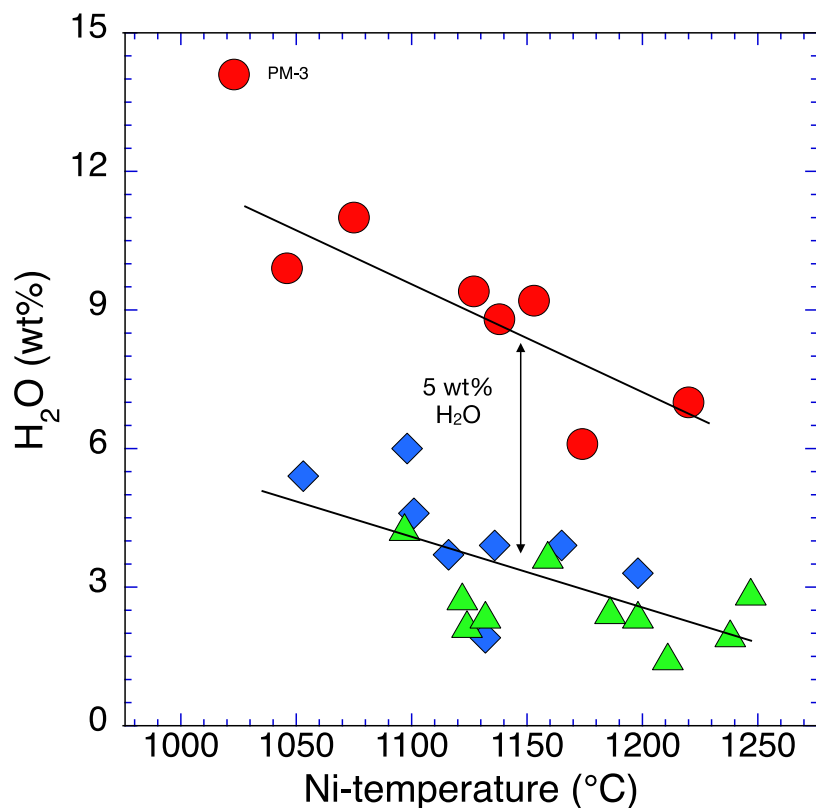


Figure 15. Calculated H₂O content in the melt (olivine-melt hygrometry) versus T_{Ni} (temperature calculated from the olivine-melt Ni-thermometer) for the Kings River samples from this study (red circles) and the Long Valley, CA basalts (blue diamonds; Jolles and Lange, 2021) and the Big Pine basalts (green diamonds; Brehm and Lange, 2020). Note that the Kings River samples plot on a distinctly different trend line (linear fit is to all samples except PM-3, which may be an outlier) compared to the Long Valley and Big Pine basalts, which overlap on different trend line (linear fit to all Long Valley and Big Pine samples). At ~1150°C, the Kings River basanites and minettes contained ~5 wt% H₂O more water than the Long Valley and Big Pine basalts. This result suggests that the Kings River samples were derived from a more refractory mantle, which required higher H₂O contents at a given temperature to form melts that could segregate and ascend to the surface, compared to the mantle source of the Long Valley and Big Pine basalts.

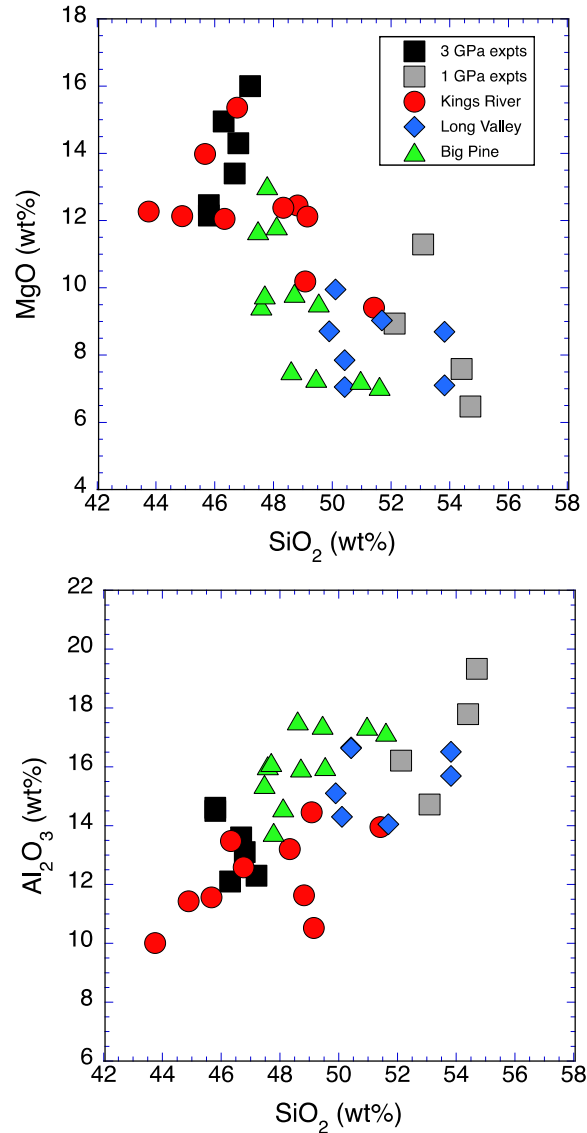


Figure 16. Plots of (a) wt% MgO versus wt% SiO₂ and (b) wt% Al₂O₃ versus wt% SiO₂ in the experimental melts from partial melting experiments on phlogopite-bearing lherzolite and harzburgite at 1 and 3 GPa (Condamine and Medard, 2014; Condamine et al., 2016). There is a clear pressure dependence to the Al₂O₃, SiO₂ and MgO contents of the experimental melts. The Kings River basanites and minettes have compositions that plot on either side of the 3 GPa experimental melts, leading to an estimated average melt segregation pressure of ~2.5-3.0 GPa (~80-100 km). In contrast, the Long Valley basalts have compositions that plot closer to ~1 GPa (vs 3 GPa) experimental melts, leading to an estimated average melt segregation pressure of ~1.5-2.0 GPa (~50-60 km). These estimates are consistent with trace element constraints that point to a garnet- vs spinel-bearing mantle source for the Pliocene southern Sierran lavas (including the Kings River volcanic field) vs the Long Valley (and Big Pine) basalts, respectively (e.g., Putirka et al., 2012).

Table 1 Whole-rock major element (wt%) and select trace element (ppm) concentrations in Kings River samples used in this study.

Sample	TD-12	MP-2	TD-17	TD-7	TD-8	PM-3	D-1	TD-4	TD-10	BcM-1
PT	BS	MN	BS	BS	BS	MN	MN	BS	TB	TB
Lat.	36°54.7'	36°50.0'	36°58.2'	36°58.5'	36°57.5'	36°53.1'	36°44.7'	37°00.0'	36°58.0'	37°00.8'
Long.	118°52.3'	118°42.6'	118°56.5'	118°50.5'	118°53.7'	119°06.2'	119°02.6'	118°50.7'	118°59.0'	118°50.2'
SiO ₂	46.76	45.67	48.82	48.33	44.89	43.75	49.15	46.33	49.08	51.42
TiO ₂	1.07	1.49	1.26	1.05	1.57	1.67	1.59	1.31	1.16	1.39
Al ₂ O ₃	12.58	11.56	11.63	13.20	11.43	10.01	10.52	13.48	14.45	13.95
FeO ^T	8.54	8.85	8.32	9.28	10.63	10.88	7.22	9.55	8.83	7.93
MnO	0.17	0.16	0.13	0.15	0.15	0.14	0.10	0.17	0.14	0.12
MgO	15.36	13.98	12.45	12.38	12.13	12.27	12.12	12.05	10.19	9.41
CaO	10.50	10.57	9.05	9.76	10.50	11.72	8.84	9.92	10.22	8.26
Na ₂ O	2.44	2.61	2.57	2.82	4.31	3.78	2.21	2.23	3.22	2.47
K ₂ O	2.06	3.90	4.38	2.23	3.04	4.38	6.61	3.40	1.87	4.02
P ₂ O ₅	0.51	1.22	1.38	0.80	1.37	1.39	1.63	1.58	0.83	1.03
LOI	1.38	0.40	0.79	0.54	0.33	0.38	1.62	0.65	0.90	0.57
Total	99.3	100.5	99.1	100.8	100.4	99.2	98.4	100.2	99.8	100.4
Ni	336	285	244	245	238	*166	303	207	138	214
Zr	140	220	345	170	254	254	370	338	152	375
Nb	6	15	16	10	16	21	21	19	10	14
Ba	1996	2870	2734	1978	2425	3719	3812	1973	1748	2363
La	34	84	58	48	66	91	83	53	59	46
MgO/SiO ₂	0.33	0.31	0.26	0.26	0.27	0.28	0.25	0.26	0.21	0.18
Mg#	0.80	0.78	0.77	0.75	0.72	0.72	0.79	0.74	0.72	0.73

Major element analyses normalized to 100%; LOI (H₂O⁺ and H₂O⁻) and original totals also shown. All major- and trace-element data are obtained by ICP-MS from Actlab Activation Laboratories and originally reported in Feldstein and Lange (1999), except Ni contents are new from this study (from XRF analyses).

*Ni content from PM-3 is from FUS-MS (fusion-mass spectrometry; not total digestion) and has larger uncertainty than Ni from XRF (± 20 vs ± 4 ppm).

PT, petrographic type; BS, basanite; MN, minette; TB, trachybasalt.

Mg# = $X_{\text{MgO}} / (X_{\text{FeO}} + X_{\text{MgO}})$ for $\text{Fe}^{3+}/\text{Fe}^{\text{T}} = 0.20$.

Table 2. Composition of most Mg-rich olivine in each sample and olivine-melt partition coefficients for Mn, Ni, and Ca

Sample	TD-12	MP-2	TD-17	TD-7	TD-8	PM-3	D-1	TD-4	TD-10	BCM-1
SiO ₂	41.29	41.71	41.87	40.92	41.63	41.47	41.65	41.64	41.19	39.94
Al ₂ O ₃	0.03	0.02	0.01	0.01	0.01	0.00	0.01	0.02	0.01	0.01
FeO ^T	9.36	8.81	9.12	11.22	8.50	10.65	7.95	9.23	10.73	16.04
MnO (calc) ^a	0.12	0.11	0.12	0.19	0.11	0.12	0.09	0.13	0.13	0.30
MgO	48.23	49.10	48.66	46.93	49.09	47.56	48.96	48.39	47.31	43.25
CaO (calc) ^b	0.11	0.09	0.11	0.11	0.10	0.11	0.10	0.15	0.09	0.16
Cr ₂ O ₃	0.03	0.06	0.06	0.01	0.06	0.03	0.04	0.04	0.04	0.02
NiO (calc) ^c	0.42	0.50	0.49	0.38	0.52	0.55	0.71	0.35	0.51	0.40
Total	99.6	100.4	100.4	99.8	100.0	100.5	99.5	100.0	100.0	100.1
Max Fo mol % ^d	90.2	90.9	90.5	88.2	91.1	88.8	91.7	90.3	88.7	82.8
D _{Mn} mol %	0.57	0.55	0.72	1.03	0.59	0.66	0.69	0.61	0.73	2.02
D _{Mg} mol % (± 0.03)	2.59	2.83	3.12	3.08	3.24	3.12	3.22	3.19	3.71	3.71
D _{Ni} mol %	8.1	11.1	13.4	10.3	16.4	21.0	14.7	10.5	21.5	13.2
	±0.3	±0.4	±0.3	±0.3	±0.4	±2.5	±0.3	±0.4	±0.6	±0.4
D _{Ca} mol % (± 0.001)	0.0087	0.00069	0.0097	0.0092	0.0076	0.0076	0.0090	0.0120	0.0070	0.0157
lnD _{Ca}	-4.744	-4.976	-4.636	-4.689	-4.880	-4.880	-4.711	-4.423	-4.962	-4.154

^a MnO (calc) from Fig. 5^b CaO (calc) from Fig. 7^c NiO (calc) from Fig. 6^d Fo mol% = (XMgO/(XMgO + XFeO))*100

Table 3a. Comparison of $^{Fe^{2+}-Mg}K_D$ (olivine-melt) at liquidus with predicted values from the literature

Calculated $^{Fe^{2+}-Mg}K_D$	TD-12	MP-2	TD-17	TD-7	TD-8	PM-3	D-1	TD-4	TD-10	BCM-1
Putirka (2016) ^a	0.33	0.32	0.32	0.33	0.31	0.31	0.31	0.32	0.33	0.33
This Study ^b	0.44	0.35	0.35	0.40	0.29	0.32	0.34	0.30	0.33	0.55
Difference	0.11	0.03	0.03	0.07	-0.03	0.01	0.03	-0.02	0.00	0.22
	fail	pass	pass	fail	pass	pass	pass	pass	pass	fail

^a K_D calculated from Eq. 8c in Putirka (2016); Error is ± 0.003

^b K_D was calculated assuming melt $Fe^{+}/FeT = 0.20$ (except TD-8) and pairing most Mg-rich olivine and whole-rock compositions (Tables 1 and 2).

^c Difference between values obtained with Putirka (2016) calculation and those measured in this study.

^d Note that redox state is estimated; K_D for TD-8 is calculated with $Fe^{3+}/FeT = 0.30$ (see text for details).

Table 3b. Comparison of $^{Fe^{2+}-Mg}K_D$ (olivine-melt) at liquidus with predicted values from the literature

Calculated $^{Mn-Mg}K_D$	TD-12	MP-2	TD-17	TD-7	TD-8	PM-3	D-1	TD-4	TD-10	BCM-1
Blundy et al. (2020) ^a	0.22	0.20	0.21	0.21	0.18	0.18	0.19	0.21	0.18	0.22
This Study ^b	0.22	0.20	0.23	0.34	0.18	0.20	0.22	0.19	0.20	0.54
Difference ^c	0.00	0.00	0.02	0.13	0.00	0.02	0.03	-0.02	0.02	0.32
	pass	pass	pass	fail	pass	pass	pass	pass	pass	fail

^a K_D calculated from Blundy et al. (2020); Error is ± 0.003

^b K_D in this study was calculated by pairing most Mg-rich olivine and whole-rock compositions (Tables 1 and 2); error is ± 0.004

^c Difference between values obtained with Blundy et al. (2020 eq. 10) calculation and those measured in this study.

Note that this test is independent of melt oxidation state; only two samples fail (TD-7 and BCM-1)

Table 4 Olivine-melt thermometry/hygrometry results

Sample	TD-12	MP-2	TD-17	TD-8	PM-3	D-1	TD-4	TD-10
No pressure correction								
$T_{Mg}(^{\circ}C)$	1368	1248	1326	1309	1323	1328	1303	1257
$T_{Ni}(^{\circ}C)$	1220	1153	1138	1075	1023	1127	1174	1047
$\Delta T = T_{Mg} - T_{Ni} (^{\circ}C)$	148	195	188	234	299	201	129	210
H ₂ O wt% (Pu et al. 2023)	7.0	9.2	8.8	11.0	13.8	9.4	6.1	9.9
H ₂ O wt% (Putirka et al., 2007)	7.0	8.5	8.1	11.4	14.6	9.4	5.4	10.3
Difference in H ₂ O wt%	0.0	0.7	0.7	-0.4	-0.8	0.2	0.7	-0.4
0.5 GPa Pressure correction								
^a $T_{Mg} (^{\circ}C)$	1395	1375	1353	1336	1350	1355	1330	1284
^b $T_{Ni} (^{\circ}C)$	1231	1164	1149	1086	1034	1138	1185	1058
$\Delta T = T_{Mg} - T_{Ni} (^{\circ}C)$	164	211	204	250	315	217	145	226
H ₂ O wt% (Pu et al. 2023)	7.7	9.9	9.6	11.8	14.5	10.2	6.8	10.6

^a Pressure correction from Herzberg and O'Hara (2002)

^b Pressure correction from Pu et al. (2023; Eq. 2)

Table 5 Clinopyroxene-liquid thermometry and barometry

Sample	TD-7	TD-10	BCM-1
Crystal	CPX-9	CPX-19	CPX-58
Texture	Dark core	Dark core	Dark core
SiO ₂	53.5	53.31	53.16
TiO ₂	0.20	0.24	0.39
Al ₂ O ₃	1.86	2.45	2.00
FeO ^T	3.93	3.81	3.95
MnO	0.10	0.09	0.10
MgO	18.15	17.6	17.87
CaO	20.84	21.47	21.26
Na ₂ O	0.52	0.52	0.42
Cr ₂ O ₃	0.92	0.75	0.96
Total	100.20	100.24	100.11
Mg#	89.2	89.2	89.0
^{FeT-Mg} Kd	0.29	0.25	0.26
P (GPa)	0.53	0.50	0.51
T (°C)	1208	1047*	1188
Depth (km)	20.0	18.9	19.3

*T_{Ni} value applied for TD-10; olivine on co-liquidus with clinopyroxene

